Thick-Layer Lead Iodide Perovskites with Bifunctional Organic Spacers Allylammonium and Iodopropylammonium Exhibiting Trap-State Emission

Eugenia Vasileiadou, Xinyi Jiang, Mikael Kepenekian, Jacky Even, Michael de Siena, Vladislav Klepov, Daniel Friedrich, Ioannis Spanopoulos, Qing Tu, Imra Tajuddin, et al.

Thick-Layer Lead Iodide Perovskites with Bifunctional Organic Spacers Allylammonium and Iodopropylammonium Exhibiting Trap-State Emission

Eugenia S. Vasileiadou, [1] Xinyi Jiang, [1] Mikaël Kepenekian,[2] Jacky Even, [3] Michael C. De Siena,[1] Vladislav V. Klepov, [1] Daniel Friedrich, [1] Ioannis Spanopoulos, [1#] Qing Tu, [4] Imra S. Tajuddin, [1] Emily A. Weiss [1] and Mercouri G. Kanatzidis [1,*]

[1] *Department of Chemistry, Northwestern University, Evanston, IL 60208, United States.*

[2] *Univ Rennes, ENSCR, CNRS, ISCR − UMR 6226, F-35000 Rennes, France.*

[3] *Univ Rennes, INSA Rennes, CNRS, Institut FOTON − UMR 6082, F-35000 Rennes, France.*

[4] *Department of Materials Science & Engineering, Texas A&M University, College Station, Texas 77840, United States*

Abstract:

The nature of the organic cation in 2D hybrid lead iodide perovskites tailors the structural and technological features of the resultant material. Herein, we present three new homologous series of (100) lead iodide perovskites with the organic cations allylammonium (AA) containing an unsaturated C=C group and iodopropylammonium (IdPA) containing iodine on the organic chain: $(AA)_2MA_{n-1}Pb_nI_{3n+1}$ (n=3-4), $[(AA)_x(IdPA)_{1-x}]_2MA_{n-1}Pb_nI_{3n+1}$ (n=1-4) and $(IdPA)_2MA_{n-1}Pb_nI_{3n+}1$ (n=1-4), as well as their perovskite-related substructures. We report the in-situ transformation of the AA organic layers into IdPA and the incorporation of these cations simultaneously into the 2D perovskite structure. Single crystal X-ray diffraction shows $(AA)_2MA_2Pb_3I_{10}$ crystallizes in the space group $P2_1/c$ with a unique inorganic layer offset (0, < ½), comprising the first example of n=3 halide perovskite with a monoammonium cation that deviates from the Ruddlesden-Popper (RP) halide structure type. $(IdPA)_2MA_2Pb_3I_{10}$ and the alloyed $[(AA)_x(IdPA)_{1-x}]_2MA_2Pb_3I_{10}$ crystallize in the RP structure, both in space group $P2_1/c$. The adjacent I···I interlayer distance in $(AA)_2MA_2Pb_3I_{10}$ is ~ 5.6 Å, drawing the $[Pb_3I_{10}]^{4-}$ layers closer together among all reported n=3 RP lead iodides. $(AA)_2MA_2Pb_3I_{10}$ presents band-edge absorption and photoluminescence (PL) emission at around 2.0 eV that is slightly redshifted in comparison to $(IdPA)_2MA_2Pb_3I_{10}$. The band structure calculations suggest both $(AA)_2MA_2Pb_3I_{10}$ and $(IdPA)_2MA_2Pb_3I_{10}$ have in-plane effective masses around 0.04.m_0 and 0.08.m_0, respectively. IdPA cations have a greater dielectric contribution than AA. The excited-state dynamics investigated by transient absorption (TA) spectroscopy reveal a long-lived (~100 ps) trap state ensemble with broadband emission; our evidence suggests that these states appear due lattice distortions induced by the incorporation of the IdPA cations.

Introduction:

Hybrid halide perovskites are low-cost semiconductors of broad technological and commercial interest as they have proven to be suitable for a wide range of applications including solar cells [1-9], light emission [10-12], radiation detection [13-17] and lasing [18-19]. The 3D halide perovskite structure: AMX_3, consists of corner-sharing MX_6 octahedra with the A-site cation occupying the center of the cuboctahedral cavities. A is one of the monovalent cations: $CH_3NH_3^+$ (MA^+), $HC(NH_2)_2^+$ (FA^+), Cs^+ or recently $CH_3NH_2NH_2^+$ [20-21], M is a divalent metal (Ge^{2+}, Sn^{2+}, Pb^{2+})[22] and X is a halide (Cl^-, Br^-, or I^-). [23-24] The incorporation of organic cations larger than the aforementioned A-site cations, leads to the dimensional reduction of the 3D structure, of general formula $(A')_m(A)_{n-1}M_nX_{3n+1}$, where A' is a monovalent (m=2) or divalent (m=1) cation and *n* is the number of inorganic layers. The resultant arrangement of alternating semiconducting inorganic layers with insulating organic layers generates a natural 2D quantum-well superlattice in a bulk crystal. This quantum confinement increases the band gap energy (E_g) and the exciton binding energy (E_b) in comparison to the 3D structures.[25-30]

The quantum-well heterostructure of the 2D perovskite can be fine-tuned by chemical synthetic design through the number of the inorganic layers *n* and the organic "spacer" cation. [31-33] Through the subsequent increase of the *n*-layer thickness in the 2D perovskite structure, the 2D materials' optical and electronic properties (E_b, E_g and photoluminescence PL) consecutively progress towards that of the 3D material.[31-32, 34-37] Elseway, the organic "spacer" cation influences indirectly the structure of the inorganic framework through its resultant non-covalent templating, as well as the intrinsic chemical properties inherited to the material such as crystallinity, solubility and thermochemical stability.[38-40] Recently, the improved environmental stability of 2D hybrid lead iodide perovskites coupled with their inherent structural flexibility,[38, 41] enabled the fabrication of robust optoelectronic devices. [6, 42-48]

The phase space of 2D halide perovskites has been populated by four primary structure subtypes, based on the charge of the organic spacer cation and the relative stacking of the inorganic layers: Ruddlesden-Popper (RP) structure $(A')_2(A)_{n-1}M_nX_{3n+1}$,[31, 49-50] Dion-Jacobson (DJ) structure $(A')(A)_{n-1}M_nX_{3n+1}$,[51-52] alternating cations in the interlayer space (ACI) type $(A')(A)_{n-1}M_nX_{3n+1}$ [53] and alkyl diammonium cations $(NH_3C_mH_mNH_3)(CH_3NH_3)_{n-1}M_nX_{3n+1}$.[54] Amongst these, the (100) RP layered halide perovskites are the most prevalent, as the majority of 2D perovskites published belong to this substructure family. [31, 34, 40, 49-52, 55] Less recurrent are layered perovskites of $n \geq 2$, incorporating functional groups (e.g. unsaturated bonds, heteroatoms) within the organic layers that diversify

significantly the explored phase space.[40, 56-68] In this context, there are also n = 1 perovskites incorporating optical active organic layers that participate in the configuration of the optical properties of the 2D perovskite.[69-72] Finally, 2D hybrid halide perovskites provide a viable architecture to perform small molecule reactivity in the solid-state by utilizing the chemical reactivity of functional organic layers to orchestrate covalent and noncovalent interactions for technological use, as in (photo)polymerization, chemisorption, electrochemical ion cycling, etc. [73-83], as well as small molecule intercalation that has been achieved with the intercalation of neutral or polarizable molecules, affording a final material with distinct structural and/or electronic properties.[57, 84-88] The inclusion of designer organic molecules with functional groups within the organic layers has been demonstrated to influence the optoelectronic and photophysical properties of 2D perovskite materials.[47, 88] Previously, the Sargent group showed that the organic cation influences the quantum well distribution, as 2D perovskite films and devices incorporating AA resulted in superior device performance due to the greatly reduced distribution of quantum wells in these materials, versus those with organic cations of similar chain length.[47] However, the synthetic preparation and structure-property relationships of crystallographically characterized thick-layer ($n \geq 2$) lead perovskites with organic cations consisting of (non-optically active) functional groups has not be investigated systematically and is of great potential interest in the community, as well as for device applications.

In this work, we incorporate the bifunctional organic molecules of allylammonium (AA) and iodopropylammonium (IdPA) to produce three new homologous series: $(AA)_2MA_{n-1}Pb_nI_{3n+1}$ (n=3-4), $[(AA)_x(IdPA)_{1-x}]_2MA_{n-1}Pb_nI_{3n+1}$ and $(IdPA)_2MA_{n-1}Pb_nI_{3n+}1$ (n=1-4). In the strongly acidic conditions of hydroiodic acid in the used synthesis, we observe the direct iodination of the allyl group with HI and its transformation into the iodopropyl group. The two distinct chemical identities of the functional groups AA (terminal alkene group) and IdPA (polarizable iodine atom), allow the drawing of several conclusions on the impact of the nature of the organic cation on the structure, optoelectronic properties and charge carrier dynamics. Single crystal X-ray diffraction reveals that $(AA)_2MA_2Pb_3I_{10}$ (n=3) crystallizes in an unexpected structure type with a unidirectional offset (0, < ½), while $(IdPA)_2MA_2Pb_3I_{10}$ and the alloyed $[(AA)_x(IdPA)_{1-x}]_2MA_2Pb_3I_{10}$ crystallize in the more conventional RP structure. $(IdPA)_2MA_2Pb_3I_{10}$ exhibits higher distortions of the equatorial Pb-I-Pb angles in comparison to $(AA)_2MA_2Pb_3I_{10}$, which leads to a blueshift of its band-edge absorption (2.03 eV versus 2.0 eV respectively) and photoluminescence (PL) emission. $(AA)_2MA_2Pb_3I_{10}$ and $(IdPA)_2MA_2Pb_3I_{10}$ manifest similarities in their electronic properties with in-plane electron and hole effective masses around 0.04.m_0 and -0.08.m_0, respectively. Additionally, the IdPA cations have a greater dielectric contribution from the iodine atom

in the organic cation, thus reducing the dielectric mismatch with the well at the origin of the dielectric confinement effect, whereas AA and BA (butylammonium: $C_4H_{12}N$) have similar dielectric contributions, dependent on the rotations of the AA cation. Furthermore, studies of the excited-state dynamics using transient absorption (TA) spectroscopy for $(AA)_2MA_2Pb_3I_{10}$, $[(AA)_{0.5}(IdPA)_{0.5}]_2MA_2Pb_3I_{10}$, $(IdPA)_2MA_2Pb_3I_{10}$ and $(BA)_2MA_2Pb_3I_{10}$ point to the formation of long-lived trap states which can account for the broadband visible-light emission observed in $(AA)_2MA_2Pb_3I_{10}$, $[(AA)_{0.5}(IdPA)_{0.5}]_2MA_2Pb_3I_{10}$ and $(IdPA)_2MA_2Pb_3I_{10}$. The trap-state emission can be correlated to the lattice distortion induced by the inclusion of the bifunctional organic molecules with their characteristic functional groups. The incorporation of the IdPA cation induces the largest lattice distortions that give rise to a new ensemble of broadband states deep into the bandgap. Notably, these deep trap states depopulate the bandedge carriers and elongate the lifetime of photoexcited carriers to ~100-ps. Such behaviors indicate the formation of a new radiative recombination pathway rooted from these functional organic spacers.

Experimental Section:

All starting materials for synthesis were purchased commercially and were used without further purification, except for Methylamine hydrochloride and Allylamine hydrochloride which were dried in an oven at 70°C. PbO (99.9%), Methylamine hydrochloride ≥ 98% ($CH_3NH_2 \cdot HCl$ = MACl), Hydroiodic acid (HI) (57 wt % in H_2O, distilled, stabilized, 99.95%) and Hypophosphorous acid solution (50 wt % in H_2O) were purchased and used as received from Sigma-Aldrich. Allylamine hydrochloride ($C_3H_5NH_2 \cdot HCl = AA^+Cl^-$) (98%) was purchased from TCI America.

Synthesis:

2-Iodopropylammonium iodide ($IdPA^+I^-$)

AA^+Cl^- (10 mmol; 1 g) is dissolved in a mixture of 8 mL HI and 0.5 mL hypophosphorous acid (H_3PO_2) by heating to boiling for four hours, under constant magnetic stirring where a clear solution was obtained. Afterwards, the solution mixture is lowered to 130°C (as stated on hotplate) until the solvent has fully evaporated and a white solid is yielded. Yield 1.53 g, (45.7%).

2D Perovskite Series with Allylamine Spacer Cation

$(AA)_2MA_2Pb_3I_{10}$ (*n*=3): PbO (2 mmol; 446 mg) and MACl (1.3 mmol; 88 mg) powders were dissolved in a mixture of 4.5 mL HI and 0.5 mL hypophosphorous acid (H_3PO_2) by heating to boiling under constant magnetic stirring, until a clear yellow solution was obtained. The reaction solution was left on the hotplate

to cool to room temperature, under continuing stirring. Next, AA^+Cl^- salt (2 mmol; 187 mg) was added to the reaction solution at room temperature (R.T.), under continuous stirring. The stirring was discontinued after 10 min, and the reaction solution was transferred to a petri dish for slow evaporation. Dark red crystals precipitated from the petri dish within 1-2 days. The crystals were isolated by vacuum filtration and dried under vacuum overnight. Yield : 189 mg, 13.7 % based on total Pb.

$(AA)_2MA_3Pb_4I_{13}$ (*n*=4): PbO (2 mmol; 446 mg) and MACl (1.5 mmol; 101 mg) powders were dissolved in a mixture of 4.5 mL HI and 0.5 mL hypophosphorous acid (H_3PO_2) by heating to boiling under constant magnetic stirring, until a clear yellow solution was obtained. The reaction solution was left on the hotplate to cool to room temperature, under continuing stirring. Next, AA^+Cl^- salt (1 mmol; 93 mg) was added to the reaction solution at room temperature (R.T.), under continuous stirring. The stirring was discontinued after 10 min and the reaction solution was transferred to a petri dish for slow evaporation. Black crystals precipitated from the petri dish within 1-2 days. The crystals were isolated by vacuum filtration and dried under vacuum overnight. Yield : 123 mg, 9.14 % based on total Pb.

2D Perovskite Series with Iodopropylamine Spacer Cation

$(IdPA)_2PbI_4$ (*n*=1): PbO (1 mmol; 223 mg) powder was dissolved in a mixture of 1.5 mL HI and 0.25 mL hypophosphorous acid (H_3PO_2) by heating to boiling under constant magnetic stirring, until a clear yellow solution was obtained. Next, $IdPA^+I^-$ salt (0.5 mmol; 93 mg) was added to the reaction solution, under continuous stirring and heating. The stirring was discontinued after 15 min and the reaction solution was left on the hotplate to cool to room temperature. Orange plate-like crystals co-precipitated from the reaction solution, along with yellow needle-like crystals of $(IdPA)_6Pb_3I_{12}$. The crystals were carefully isolated from the second-phase crystals, removed from the HI mother liquid by vacuum filtration and dried under vacuum overnight. Yield : 34 mg, 3.13 % based on total Pb.

$(IdPA)_2MAPb_2I_7$ (*n*=2): PbO (2 mmol; 446 mg) and MACl (1 mmol; 70 mg) powders were dissolved in a mixture of 4.5 mL HI and 0.5 mL hypophosphorous acid (H_3PO_2) by heating to boiling under constant magnetic stirring, until a clear yellow solution was obtained. Next, $IdPA^+I^-$ salt (2 mmol; 372 mg) was added to the reaction solution, under continuous stirring and heating. The stirring was discontinued after 15 min and the reaction solution was left on the hotplate to cool to room temperature. Bright red crystals precipitated from the reaction solution. The crystals were isolated by vacuum filtration and dried under vacuum overnight. Yield : 132 mg, 15.47 % based on total Pb.

$(IdPA)_2MA_2Pb_3I_{10}$ (*n*=3): PbO (2 mmol; 446 mg) and MACl (1.3 mmol; 88 mg) powders were dissolved in a mixture of 4.5 mL HI and 0.5 mL hypophosphorous acid (H_3PO_2) by heating to boiling under constant magnetic stirring, until a clear yellow solution was obtained. Next, $IdPA^+I^-$ salt (2 mmol; 372 mg) was added to the reaction solution, under continuous stirring and heating. The stirring was discontinued after 15 min and the reaction solution was left on the hotplate to cool to room temperature. Dark red crystals precipitated from the reaction solution. The crystals were isolated by vacuum filtration and dried under vacuum overnight. Yield : 243 mg, 15.66 % based on total Pb.

$(IdPA)_2MA_3Pb_4I_{13}$ (*n*=4): PbO (4 mmol; 892 mg) and MACl (3 mmol; 202 mg) powders were dissolved in a mixture of 8 mL HI and 0.5 mL hypophosphorous acid (H_3PO_2) by heating to boiling under constant magnetic stirring, until a clear yellow solution was obtained. Next, $IdPA^+I^-$ salt (2 mmol; 372 mg) was added to the reaction solution, under continuous stirring and heating. The stirring was discontinued after 15 min and the reaction solution was left on the hotplate to cool to room temperature. Black crystals precipitated from the reaction solution. The crystals were isolated by vacuum filtration and dried under vacuum overnight. Yield : 356 mg, 12.08 % based on total Pb.

2D Perovskite Series with Mixed Spacer Cations (Allylamine + Iodopropylamine)

$[(AA)_x(IdPA)_{1-x}]_2PbI_4$ (*n*=1): PbO (1 mmol; 223 mg) powder was dissolved in a mixture of 1.5 mL HI and 0.25 mL hypophosphorous acid (H_3PO_2) by heating to boiling under constant magnetic stirring, until a clear yellow solution was obtained. Next, AA^+Cl^- salt (2 mmol; 187 mg) was added to the reaction solution, under continuous stirring and heating. The stirring was discontinued after 5 min and the reaction solution was left on the hotplate to cool to room temperature. Yellow plate-like crystals co-precipitated from the reaction solution, along with yellow needle-like crystals.

$[(AA)_x(IdPA)_{1-x}]_2MAPb_2I_7$ (*n*=2): PbO (2 mmol; 446 mg) and MACl (1 mmol; 70 mg) powders were dissolved in a mixture of 3.5 mL HI and 0.5 mL hypophosphorous acid (H_3PO_2) by heating to boiling under constant magnetic stirring, until a clear yellow solution was obtained. Next, AA^+Cl^- salt (2 mmol; 187 mg) was added to the reaction solution, under continuous stirring and heating. The stirring was discontinued after 5 min and the reaction solution was left on the hotplate to cool to room temperature. Red crystals precipitated from the reaction solution. The crystals were isolated by vacuum filtration and dried under vacuum overnight.

$[(AA)_x(IdPA)_{1-x}]_2MA_2Pb_3I_{10}$ (*n*=3): PbO (3 mmol; 669 mg) and MACl (2 mmol; 135 mg) powders were dissolved in a mixture of 5 mL HI and 0.5 mL hypophosphorous acid (H_3PO_2) by heating to boiling under

constant magnetic stirring, until a clear yellow solution was obtained. Next, AA^+I^- salt (2 mmol; 187 mg) was added to the reaction solution, under continuous stirring and heating. The stirring was discontinued after 5 min and the reaction solution was left on the hotplate to cool to room temperature. Dark red crystals precipitated from the reaction solution. They were isolated by vacuum filtration and dried under vacuum overnight.

$[(AA)_x(IdPA)_{1-x}]_2MA_3Pb_4I_{13}$ (*n*=4): PbO (1 mmol; 223 mg) and MACl (0.75 mmol; 55 mg) powders were dissolved in a mixture of 1.5 mL HI and 0.25 mL hypophosphorous acid (H_3PO_2) by heating to boiling under constant magnetic stirring, until a clear yellow solution was obtained. Next, AA^+I^- salt (1 mmol; 93 mg) was added to the reaction solution, under continuous stirring and heating. The stirring was discontinued after 5 min and the reaction solution was left on the hotplate to cool to room temperature. Black crystals precipitated from the reaction solution. They were isolated by vacuum filtration and dried under vacuum overnight.

Characterization:

The experimental techniques and methods used for the characterization of the structure and properties of the studied materials are found in detail in the Supporting Information (**S.I.**).

Results and Discussion:

Synthetic Aspects and Reactivity of Allylammonium Cation in Hydroiodic Acid (57% w/w):

The ability of two different organic spacer cations to stabilize the 2D RP structures was investigated in this work. The first cation, AA, resulting from the dissolution of allylamine in concentrated HI underwent iodination across the unsaturated C=C bond with heating to yield the second cation iodopropylamine, IdPA. This reaction is being discussed in detail later. **Figure 1** and **Table 1** shows a structural and compositional overview the fourteen new 2D perovskites incorporating organic spacer cations with functional groups, synthesized in this work. The spacer cations employed here, allylammonium ($H_2C{=}CH{-}CH_2{-}NH_3^+$ or C_3H_8N) and 2-iodopropylammonium ($H_3C{-}CH(I){-}CH_2{-}NH_3^+$ or C_3H_9NI), consist of a core alkylammonium skeleton of three carbons, where AA inheres a terminal alkene group and IdPA contains an iodine heteroatom on the alkylammonium chain. The targeted synthesis of the studied thick-layer perovskites was developed on the solution method based on aqueous hydroiodic acid. In brief, stoichiometric concentration of the starting reagents PbO, MACl and organic spacer is used to obtain uniform phase product of desired *n* value. As a result of the highly soluble nature of the organic

cations employed here, stoichiometric amount of the organic spacer is used. This is also the case for the saturated version of the AA cation in the Ruddlesden-Popper series with propylammonium (PrpA: $C_3H_{10}N$) as the organic spacer cation, as well as in the series of alternating cation in the interlayer space with guanidinium (GA: CH_6N_3).[49, 53] In contrast, the synthesis of other series of 2D lead iodide perovskites that incorporate longer alkylammonium cations as the organic layers, require the off-stoichiometry method developed by our group.[31, 50-52, 54]

The synthetic exploration and incorporation of functional groups into the organic layers of the 2D hybrid halide perovskite structure needs to be carefully considered before progressing to the targeted synthesis of the thick-layer (n>2) perovskite series. The established synthetic protocol based on the solution method with boiling, aqueous hydroiodic acid has been systematically used for the bulk synthesis of the majority of thick-layer lead iodide perovskites reported to date, as a universal method. [31, 50-54] In our case, the terminal alkene group in the allylammonium cation is prone to electrophilic addition. To our knowledge, literature review upon the exact reaction conditions of the terminal alkene-ammonium molecules in aqueous hydroiodic acid (without additive reagents) and its products, are not well studied.[89-94] Aqueous hydroiodic acid has not been reported on extensively in the synthesis of organic aminoiodides. For context, the direct addition of anhydrous HI (hydroiodination) to alkenes and alkynes for the synthesis of organic iodides is avoided due to difficulty of controlling iodine liberation, which leads to side reactions and poor yields.[90] Instead, alternative materials and metals are used that generate HI in situ, although these reagents in majority, are expensive.[89-94]

To understand the reactive behavior of the allylammonium cation (also known as propenyl-ammonium) in hydroiodic acid as in our synthetic protocol (which employs a solution mixture of HI/H_2PO_3), NMR experiments were carried out on AA solely with HI, mimicking the conditions of the different steps of the perovskite synthesis (**Figure S19)**. Firstly, AA^+Cl^- salt was dissolved in aqueous HI at room temperature (R.T.). The characteristic protons peaks corresponding to the unsaturated carbons of AA at 5.3 - 5.8 ppm are present in the ^1H NMR spectra, with no peaks corresponding to the addition product of IdPA. Additionally, the ^{13}C NMR spectrum displays two peaks present in the 100 ppm region, indicating clearly that the unsaturated carbon bond did not react in aqueous HI at R.T. for up to three weeks (**Figure S20**). These results agree with previous studies, which do not report reactivity for simple addition reactions of alkenes in aqueous hydrobromic acid at low temperature.[79, 83] Next, AA^+Cl^- salt was dissolved in boiling, aqueous hydroiodic acid under stirring for 5 min, as done in our established

perovskite synthetic protocol. Here, the ^{1}H NMR shows the characteristic proton peaks of AA in the 5.3 - 5.8 ppm range, as well as peaks corresponding to IdPA in 1.8 - 4.2 ppm range. Interestingly, after one month, the aforementioned solution's NMR shows a larger amount of IdPA, as it seems that the heat catalyzes the production of IdPA within a month-time period (**Figure S21**). Lastly, we dissolved the $AA^{+}Cl^{-}$ salt in boiling hydroiodic acid under stirring for 30 min. In this case, both organic cations exist, with IdPA present in roughly over 90% of the product mixture. Consequently, AA fully reacts with aqueous HI, under constant heating. NMR confirms the almost full conversion of AA to 2-iodopropylammonium, with a small byproduct of the 1-iodopropylammonium salt corresponding to the remaining peaks (**Figure S22**). 2-iodopropylammonium (IdPA) is the Markovnikov product of the electrophilic addition of aqueous HI.

The above experiments demonstrate that the unsaturated bond of the AA cation can be preserved in aqueous HI solution at R.T. but will react upon heating. This requires modification of the conditions of the established synthetic protocol, with the reaction solution being left at R.T. and then, proceeding to add the AA organic spacer cation to the reaction solution. In our previously established synthetic protocol, the reaction solution is heated to boiling in order to create a reflux system, which is followed by the cooling of the reaction solution by returning to R.T. The temperature difference facilitates the immediate precipitation of the layered perovskite crystals. Based on the targeted 2D perovskite material, adjusting appropriately the cooling rate of the reaction solution assists the growth of higher quality crystals. In the solution synthesis of the series $(AA)_2MA_{n-1}Pb_nI_{3n+1}$ (n=3 and 4) with aqueous hydroiodic acid, heating cannot be introduced to the system. As such, in order to expedite the growth of 2D perovskite crystals, the reaction solution is transferred to a large surface petri-dish to assist the quick evaporation of solvent. As a result, the growth of high-quality crystals of the $(AA)_2MA_{n-1}Pb_nI_{3n+1}$ (n=3 and 4) series is difficult to control based on this solution synthesis with aqueous hydroiodic acid. Surprisingly, targeted synthesis of n=1 and n=2 did not yield the expected 2D perovskites. Instead 2D structures of alternating corner- and face-sharing $[PbI_6]^{4-}$ octahedra were formed, similarly to the behavior of the saturated analogue with the PrpA cation[49] (**Figure 1**). Detailed analysis of these structures is in the *Crystal Structures* section below.

Capitalizing on the chemistry accessible through the terminal unsaturated bond of the allylammonium cation, the targeted synthesis of the $(IdPA)_2MA_{n-1}Pb_nI_{3n+1}$ (n=1-4) series was achieved, to further investigate the role of a heteroatom functional groups in the organic layers. Since, the IdPA salt is not commercially available and coupled with our NMR studies, the synthesis of the salt was realized

by prolong heating of allylammonium in aqueous HI/H_3PO_2. Based on the circular dichroism (CD) spectra (**Figure S18**), the $(IdPA)_2MA_{n-1}Pb_nI_{3n+1}$ (n=1-4) homologous series contain a racemic mixture of the IdPA cation. This is expected as the starting alkene-amine, allylammonium, has no chiral center. The addition reactions of alkenes with no stereogenic center produces a racemic mixture of two enantiomers.[95] Thus, the synthesis of amino organoiodides can be accomplished simply, practically and without expensive additional reagents. A general study on this hydroiodination method and its regioselectivity could be of benefit for the synthesis of a wide range of amino-alkyl and amino-alkenyl iodides, which are important building blocks in organic synthesis.

The synthesis of 2D perovskites with IdPA serving as the organic spacers gives the full thick-layer perovskite series (n= 1-4). However, $(IdPA)_2PbI_4$ (n=1) is the kinetic product, as its targeted synthesis instead yields a 0D perovskitoid with the formula $(IdPA)_6Pb_3I_{12}$ = $(IdPA)_2PbI_4$ (**Figure 1**). Stoichiometrically, $(IdPA)_6Pb_3I_{12}$ composition is equivalent to the n=1 layered perovskite but the structure differs drastically, which consists of a trimer of face-sharing $[PbI_6]^{4-}$ octahedra partitioned by the IdPA cations (**Figure 1**). In the targeted synthesis of $(IdPA)_2PbI_4$ (n=1), crystals of the layered $(IdPA)_2PbI_4$ perovskite precipitate, but within hours convert to crystals of 0D $(IdPA)_6Pb_3I_{12}$. Therefore, 0D $(IdPA)_6Pb_3I_{12}$ is the thermodynamically favored product, corroborated by the fact it is more dense (Volume/Density = 865.1) than $(IdPA)_2PbI_4$ (Volume/Density = 326.8). Recently, a similar crystal-to crystal transformation was reported in a n=1 perovskite with cysteamine.[96] Furthermore, a second byproduct forms, that of a 1D perovskitoid with the formula $(IdPA)PbI_3$. It belongs to the NH_4CdCl_3 structure-type, consisting of a 1D double ribbon of face- and edge-sharing $[PbI_6]^{4-}$ octahedra (**Figure 1**). This 1D structure was observed as well with $(GA)PbI_3$.[53] It is interesting how the AA and IdPA cations yield non-perovskite structures similar with GA and PrpA, as a result of the short size, steric and hydrogen bonding (HB) interactions. The greater HB capabilities of the organic layers unlock a rich structural diversity of perovskite-related compounds, providing synthetic clues for chemical exploration of new structural motifs.

Availing from the reactivity accessible from the terminal unsaturated bond of the AA cation, it is possible to create in-situ, a solid solution incorporating two chemically distinct cations in the A' position of the 2D perovskite structure, which has not been reported before in bulk, thick-layer perovskites (n >2), to our knowledge. With monitored heating, the AA cation reacts in the perovskite synthesis and slowly converts to IdPA, bestowing the 2D perovskite series of $[(AA)_x(IdPA)_{1-x}]_2(MA)_{n-1}Pb_nI_{3n+1}$ (n=1-4), which consists of both AA and IdPA cations in the organic layers. The combination of PXRD (**Figure S1-S11**)

and NMR (**Figure S14-S24**) data are necessary to probe the products of the in-situ reactions of the organic layers, to avoid inaccurate characterization of the organic and/or inorganic components.[97] Progressively incorporating the IdPA cations into the organic layers affords a final A' site mixed-cation perovskite product with an increase in the stacking axis length and interlayer distance of the $[(AA)_x(IdPA)_{1-x}]_2(MA)_{n-1}Pb_nI_{3n+1}$ (n=3-4) series versus the $(AA)_2MA_{n-1}Pb_nI_{3n+1}$ (n=3 and 4) series (**Figure 2C-D**). Withal, NMR helps identify the organic cations present in the 2D material, which are assigned based on the characteristic peaks of the functional groups of the organic chains. This strategy of in-situ reaction of the organic layers appends an additional structural parameter to tune in the structure-property relationship of 2D perovskites.

The powder X-ray diffraction (PXRD) patterns of crystals $(AA)_2MA_{n-1}Pb_nI_{3n+1}$, $(IdPA)_2MA_{n-1}Pb_nI_{3n+1}$ and $[(AA)_x(IdPA)_{1-x}]_2MA_{n-1}Pb_nI_{3n+1}$ (n=3 and 4) is shown in **Figure 2A-B**, with negligible reflections from secondary phases to confirm the successful synthesis of the studied compounds (**Figure 2A-B** and **Figure S3-S6,S9-S11)**. The d-spacing for the low angle peaks (below the characteristic 3D $MAPbI_3$ reflections $\sim 2\theta$=13°) corresponds to the distance from the center of each layer, allowing us to easily estimate the expected peak positions for specific n-layer thickness, as well as the identity of the organic spacer cation (**Table 1**). For $(AA)_2MA_2Pb_3I_{10}$ (n=3) - $(AA)_2MA_3Pb_4I_{13}$ (n=4), the d_{100} spacing of the first reflections are at ~24.2 Å and ~30.5 Å respectively, whereas for $(IdPA)_2MA_2Pb_3I_{10}$ (n=3) - $(IdPA)_2MA_3Pb_4I_{13}$ (n=4) the d_{100} spacing is ~26.9 Å and ~32.1 Å respectively. The d_{100} spacing of the first reflection for the solid solution $[(AA)_x(IdPA)_{1-x}]_2MA_{n-1}Pb_nI_{3n+1}$ (n=3 and 4) is between the range of 24.2 - 26.9 Å for n=3 members, and between 30.5 – 32.1 Å for n=4 members.

All three series of the novel 2D perovskites studied here, demonstrate a similar characteristic in crystal morphology of naturally forming clumps of crystals, composed of smaller single crystals with plate-like shape. The crystal clumps have overall irregular shapes and easily fracture during the task of isolation of the single crystals. SEM studies illustrate the plate-like morphology of the single crystals as well as the stacking-layered morphology for all studied materials (**Figure S30-S32**), which is a distinctive characteristic for the 2D layered perovskite structure. In comparison, although the structural parameters (stacking axis and interlayer distance) of $(IdPA)_2MA_{n-1}Pb_nI_{3n+1}$ (n=1-4) are similar to $(BA)_2MA_{n-1}Pb_nI_{3n+1}$ (n=1-4), the crystal morphology of the IdPA series is drastically different from BA and resembles closely to AA, based on qualitative observation. We employed nanoindentation of $(AA)_2MA_2Pb_3I_{10}$ single crystals (i.e., n = 3) along the stacking axis and compared the obtained elastic modulus and hardness to

those from BA- and alkyl diammonium-based 2D lead iodide layered perovskites with the same n number (**Table S1**). We found that although both containing non-covalent interfaces between adjacent organic spacer molecular layers inside the crystals, $(AA)_2MA_2Pb_3I_{10}$ is stiffer (elastic modulus E = 5.74 ± 0.48 GPa) than their BA counterpart, $(BA)_2MA_2Pb_3I_{10}$ (E = 4.40 ± 0.57 GPa),[98] but softer than the diammonium 2D perovskite $(NH_3C_8H_{16}NH_3)MA_2Pb_3I_{10}$ (E = 11.65 ± 1.76 GPa).[99] This is probably due to the additional hydrogen-bonding interaction between the terminal group C=C in the spacer molecules, which is stronger than the pure van der Waals bonding between the terminal methane group CH_3 in $(BA)_2MA_2Pb_3I_{10}$, but weaker than the covalent bonding in $(NH_3C_8H_{16}NH_3)MA_2Pb_3I_{10}$. This further confirms that tuning the interactions between the 2D perovskite layers can be an effective approach to tailor the mechanical behavior of 2D perovskites, as suggested by some of us in earlier publications.[99-101] The obtained hardness values (i.e., the resistance to plastic deformation) generally follow the same trend of elastic modulus, though the difference between $(AA)_2MA_2Pb_3I_{10}$ and $(BA)_2MA_2Pb_3I_{10}$ is less dramatic. The rich compositional parameter space and associated interesting new structures (details in the following section) of the three series of novel 2D perovskites reported here calls for a thorough investigation of their mechanical properties to study the structure-mechanical property relationship of 2D RP perovskites as a function of the organic component [98, 100, 102-104] and establish guidelines for materials design to improve the mechanical stability issues of 2D perovskites.[101]

Description of Crystal Structures:

The structures of all three series: $(AA)_2MA_2Pb_3I_{10}$ (n=3), $[(AA)_x(IdPA)_{1-x}]_2(MA)_{n-1}Pb_nI_{3n+1}$ (n=1-3) and $(IdPA)_2MA_{n-1}Pb_nI_{3n+1}$ (n=1-3) were solved from single crystal X-ray diffraction (SCXRD) data collected at room temperature (**Table 2, Table 3** and **Table S2-S3)**. These phases consist of corner sharing $[PbI_6]^{4-}$ octahedra, separated by the organic spacer cations in the [100] direction (**Figure 1**). The chemical identity of the organic layers is distinctive in the 2D perovskite series under study, by virtue of the characteristic functional groups embodied onto the identical, core alkylammonium chain. The incorporation of functional groups into the organic layers affords significant structural variances between the crystal structures with the same n-layer thickness. On the account for the consistent comparison amongst all three series, we will focus the discussion on the structural analysis of the n=3 members: $(AA)_2MA_2Pb_3I_{10}$, $(IdPA)_2MA_2Pb_3I_{10}$ and $[(AA)_x(IdPA)_{1-x}]_2MA_2Pb_3I_{10}$.

The crystal structure of $(AA)_2MA_2Pb_3I_{10}$ (n=3) consists of $[Pb_3I_{10}]^{4-}$ inorganic layers that are alternated with AA organic layers. The electrostatic interactions between the organic-inorganic layers

yields a three-layer perovskite structure in which the inorganic layers stack on top of each other, along the stacking axis *a* (**Figure 3A**). Hence, there is no offset of the consecutive inorganic layers, along the *a* stacking axis with respect to the *bc* plane (**Figure 3A**). Along the *b* stacking axis with respect to the *ac* plane, there is an offset < ½. Therefore, $(AA)_2MA_2Pb_3I_{10}$ (*n*=3) is a new, unique structure type, different from the Ruddlesden-Popper (RP) type with offset (½,½) and the Dion-Jacobson (DJ) type with offset (0,0), (0,½). This is the first report of a monoammonium cation affording a non-RP hybrid halide structure type, which is evidently due to the additional hydrogen-bonding (HB) interactions induced from the terminal C=C, alkene group in the allylammonium cation. A comparison of the crystal structures $(AA)_2MA_2Pb_3I_{10}$ and $(PrpA)_2MA_2Pb_3I_{10}$ (*n*=3), which consists of organic layers with the saturated cation propylammonium,[49] evinces the definite effect of the terminal alkene group on the resultant 2D perovskite structure (**Figure 3**). $(PrpA)_2MA_2Pb_3I_{10}$ (*n*=3) adopts the RP structure with the staggered arrangement of the successive $[Pb_3I_{10}]^{4-}$ inorganic layers (**Figure 3A**).[49] Furthermore, the stacking axis of $(AA)_2MA_2Pb_3I_{10}$ is 0.97Å ≈ 1Å smaller than that of $(PrpA)_2MA_2Pb_3I_{10}$ (**Figure 4A**), while the interlayer distance (between the successive inorganic layers) and adjacent I···I distance of $(AA)_2MA_2Pb_3I_{10}$ is 0.76Å and 1.18 Å smaller respectively than that of $(PrpA)_2MA_2Pb_3I_{10}$ (**Figure 4B**).

The systematically smaller values in the structural parameters of $(AA)_2MA_2Pb_3I_{10}$ versus $(PrpA)_2MA_2Pb_3I_{10}$ is surprising, as the only difference in the composition of the two materials is the terminal unsaturated bond in AA cation (C=C bond length ~ 1.34 Å) versus the saturated PrpA cation (C-C bond length ~ 1.54 Å). This is likely the result of the terminal alkene bond's: (i) greater HB interactions between the organic-organic and organic-inorganic layers due to the C=C group in the organic layers, (ii) small steric interactions and (iii) short size of AA cation, which is the smallest known monoammonium cation to template the 2D halide perovskite structure. The collective effect of the described electrostatic interactions brings the successive inorganic layers significantly closer together due to the AA layers and the 2D structure is sustained through the more rigid stacking of the inorganic layers with unidirectional offset (0,<1/2), deviating substantially from the RP structure. Thus, a synthetic exemplar is corroborated for the targeted synthesis of RP and DJ hybrid halide perovskites: an organic spacer cation with high HB capabilities, negligible steric hinderance and small cation size, leads to reduced spacing of the organic layers and a tendency to align of the successive inorganic layers to produce a 2D structure close to that of DJ or ACI perovskites. Only cyclic and aromatic diammonium cations have templated the 2D DJ halide perovskite structure, thus far based on structural characterization, confirming the synthetic criterion discussed. Lastly, the AA and PrpA cations behave similarly for members *n*<2, by

producing the same "step-like" homologous series of non-perovskites $(B)_{2m+4}(MA)_{m-2}Pb_{2m+1}I_{7m+4}$ (m = 1-4), where the $[PbI_6]^{4-}$ octahedra connect in 2D through a corner- and face-sharing motif (**Figure 1**).[49]

The crystal structure of $(IdPA)_2MA_2Pb_3I_{10}$ (n=3) consists of $[Pb_3I_{10}]^{4-}$ inorganic layers that are alternated with IdPA organic layers, where there is an iodine atom on the second carbon of the propylammonium skeleton (**Figure 3**). The presence and position of the iodine atom on the alkylammonium cation induces greater steric interactions and bulkiness within the organic layers. Consequently, the RP structure is templated with two offset layers per unit cell, verifying again the proposed synthetic exemplar. Lastly, single crystal X-ray diffraction of $(IdPA)_2MAPb_2I_7$ (n=2) and $(IdPA)_2PbI_4$ (n=1) reveals that these members of the $(IdPA)_2MA_{n-1}Pb_nI_{3n+1}$ series, also belong to the RP structure family (**Figure 1**).

Furthermore, to institute a directory of synthetic criterion for the predictive synthesis and rational design of halide perovskite semiconductors, it is essential to collate insightfully the structural information of (i) RP lead iodide perovskites with the smallest monoammonium cations [PrpA and BA=butylammonium] and the other known structure types that are (ii) DJ based on dications such as $(3AMP)MA_2Pb_3I_{10}$, $(4AMP)MA_2Pb_3I_{10}$, $(3AMPY)MA_2Pb_3I_{10}$ and $(4AMPY)MA_2Pb_3I_{10}$ where AMP = *a*-(aminomethyl)piperidinium, AMPY = *a*-(aminomethyl)pyridinium], and (iii) the ACI materials such as $(GA)MA_3Pb_3I_{10}$ with two different monocations in the interlayer and a DJ-like (0,1/2) offset and finally (iv) the primary diammonium cations $[(NH_3C_8H_{16}NH_3)(MA)_2Pb_3I_{10}$ and $(NH_3C_9H_{18}NH_3)(MA)_2Pb_3I_{10}$, close to the RP class in terms of offset.[51-54]

Amongst the RP lead iodide perovskites with the smallest monoammonium cations, $(AA)_2MA_2Pb_3I_{10}$, $[(AA)_x(IdPA)_{1-x}]_2MA_2Pb_3I_{10}$, $(IdPA)_2MA_2Pb_3I_{10}$, $(PrpA)_2MA_2Pb_3I_{10}$ and $(BA)_2MA_2Pb_3I_{10}$ are examined comparatively. In **Figure 4A**, $(AA)_2MA_2Pb_3I_{10}$ has the smallest stacking axis and interlayer distance among the n=3 compounds under study, followed by $(PrpA)_2MA_2Pb_3I_{10}$ < $(BA)_2MA_2Pb_3I_{10}$ < $[(AA)_x(IdPA)_{1-x}]_2MA_2Pb_3I_{10}$ < $(IdPA)_2MA_2Pb_3I_{10}$. The significantly smaller values of the structural parameters of $(AA)_2MA_2Pb_3I_{10}$ shows that AA brings the inorganic $[PbI_6]^{4-}$ layers closer together, which reflects the strong impact of the electrostatic influences from the terminal alkene group, as discussed above. In comparison, $(PrpA)_2MA_2Pb_3I_{10}$ and $(BA)_2MA_2Pb_3I_{10}$ have an expected evolution of their structural parameters. $[(AA)_x(IdPA)_{1-x}]_2MA_2Pb_3I_{10}$ operates as a median compound, to affirm the smooth evolution of the structural parameters from $(AA)_2MA_2Pb_3I_{10}$ to $(IdPA)_2MA_2Pb_3I_{10}$, proving to have a higher composition of IdPA cations and thus, resembling more $(IdPA)_2MA_2Pb_3I_{10}$.

$(IdPA)_2MA_2Pb_3I_{10}$ has the largest interlayer distance among the examined *n*=3 compounds, even compared to $(BA)_2MA_2Pb_3I_{10}$, owning to the steric interaction and bulkiness of the C-I bond (~ 2 Å) (**Figure 4A)**.

Figure 4C-D demonstrates the comparison of the main structural parameters of $(AA)_2MA_2Pb_3I_{10}$ individually, along with the above RP structures with small monoammonium cations, as well as with DJ, ACI and diamine structure types. The ACI and DJ structures have significantly the smallest interlayer and adjacent I···I distances amongst all the structure types collated here, with $(AA)_2MA_2Pb_3I_{10}$ following behind. The RP and diamine structure types have similar values of their interlayer and adjacent I···I distances. Hence, the HB capabilities and steric interactions of the organic layers produce profound variance in the structural parameters, such as the offset type, and especially on the interlayer and adjacent I···I distances.

Regarding the Pb-I-Pb angles, there are two sorts classified: the equatorial angle (parallel to the inorganic plane) and the axial angle (in the stacking direction). The distortion level of the Pb-I-Pb angles of the inorganic octahedra is correlated with the bandgap of the material, as it is an important parameter in the calculation of the electronic structure of the material.[105-107] As seen in **Figure 5A**, the distortion levels of the Pb-I-Pb angles are similar for $(AA)_2MA_2Pb_3I_{10}$, $(PrpA)_2MA_2Pb_3I_{10}$ and $(BA)_2MA_2Pb_3I_{10}$. In contrast, $[(AA)_x(IdPA)_{1-x}]_2MA_2Pb_3I_{10}$ and $(IdPA)_2MA_2Pb_3I_{10}$ have significantly greater deviation of their Pb-I-Pb angles comparatively (**Figure 5A**). The iodine atom of the IdPA cation has a preference to instigate greater distortion of the equatorial Pb-I-Pb angle versus the axial angle, which exhibits the smallest amount of distortion among the examined *n*=3 RP compounds. Moreover, the equatorial (eq.) angles can be split into eq. angles of the outer inorganic layers and eq. angles of the inner inorganic layer (**Figure 5B**). Comparatively among both groups, the sequence of angle distortion is $(IdPA)_2MA_2Pb_3I_{10} \approx [(AA)_x(IdPA)_{1-x}]_2MA_2Pb_3I_{10} > (AA)_2MA_2Pb_3I_{10} \approx (PrpA)_2MA_2Pb_3I_{10} > (BA)_2MA_2Pb_3I_{10}$. Again, $[(AA)_x(IdPA)_{1-x}]_2MA_2Pb_3I_{10}$ and $(IdPA)_2MA_2Pb_3I_{10}$ exhibit the greatest distortions due to the steric interaction of the iodine atom within the organic layers. $(AA)_2MA_2Pb_3I_{10}$ and $(PrpA)_2MA_2Pb_3I_{10}$ have comparable values of inner and outer eq. angles, although on average $(AA)_2MA_2Pb_3I_{10}$ has slightly larger distortion. Lastly, $(BA)_2MA_2Pb_3I_{10}$ has the smallest level of distortion in general, for both inner and outer eq. angles. Therefore, the greater HB and smaller steric interactions of the AA cation govern the stacking geometry of the inorganic layers but does not induce profound variance in the distortion levels of the equatorial Pb-I-Pb, in comparison with PrpA and BA. This implies that the strength of the electrostatic

interactions of the spacer cation is balanced between its control on the stacking geometry of the inorganic layers and the distortion level within the inorganic layers.

Figure 5C displays the equatorial and axial Pb-I-Pb angles among the *n*=3 compounds across the different structure types RP, DJ, ACI and diamine-based lead iodide perovskites. For the crucial eq. Pb-I-Pb angles, the sequence of greater distortion is as following: DJ > RP > AA > Diamine >ACI. This result coupled with the structural information on the interlayer distances and the observed band gap values, leads to a fundamental conclusion. The close proximity of the $[PbI_6]^{4-}$ layers in hybrid halide perovskites suggests a greater contribution on the band gap value than the distortion level of the eq. Pb-I-Pb angles, as is verified by the observed band gaps. ACI has the smallest interlayer distance and smallest distortions of the eq. Pb-I-Pb angles, which logically aligns with the observed lowest Eg value. Although, the DJ perovskites have the highest distortions in the eq. Pb-I-Pb angles, their average Eg value are lower than those of RP and diamines, which have smaller distortions. As mentioned above, the average value of the interlayer distance in DJ perovksites is amongst the smallest in comparison. Hence, this indicates that the adjacent $[PbI_6]^{4-}$ layers interact electronically and must have an electronic contribution to the bandgap value, when in significantly close proximity, where the trend in bandgap established thus far shows that bandgap of ACI < DJ < RP ≈ Diamine. [51-54, 108] The proximity is regulated by the choice of the organic spacer cation, providing new insight for targeted design synthesis criterion.

Optical Properties:

The absorption spectra are typical of layered perovskites, with an absorption edge and an excitonic peak above the bandgap due to quantum confinement. The bandgaps are estimated by extrapolating from the absorption edge, a slope perpendicular to the x axis. **Figure 6A** depicts the absorption spectra of the *n*=3 and *n*=4 members of the AA, IdPA and AA/IdPA mixed-cation series. It is noteworthy that exciton signatures do not clearly appear in these spectra, which can be either qualitatively be attributed to a small exciton binding energy or to the crystalline powder morphology leading to a very large inhomogeneous broadening of the exciton resonances (**Figure 6A** and **Figure 6C)**. The bandgap of $(AA)_2MA_2Pb_3I_{10}$ (*n*=3) and $(AA)_2MA_3Pb_4I_{13}$ (*n*=4) are 2.00 eV and 1.91 eV, respectively; both compounds exhibit slightly lower E_g values respectively than their analogues: $(IdPA)_2MA_2Pb_3I_{10}$ (2.03 eV) and $(IdPA)_2MA_3Pb_4I_{13}$ (1.99 eV) respectively (**Figure 6B)**. This trend is also apparent in the PL spectra: the band-edge emission of has energy 1.99 eV for $(AA)_2MA_2Pb_3I_{10}$ and 1.90 eV for $(AA)_2MA_3Pb_4I_{13}$, both of which are red-shifted from that of their analogs $(IdPA)_2MA_2Pb_3I_{10}$ (2.02 eV) and $(IdPA)_2MA_3Pb_4I_{13}$ (1.92 eV) (**Figure 6D)**.

The emission of $(AA)_2MA_2Pb_3I_{10}$ is lower energy than the emission of $(IdPA)_2MA_2Pb_3I_{10}$ due to the coupled effects of smaller distortions of the eq. Pb-I-Pb angles and smaller interlayer distance, as discussed above (**Figure 2** and **Figure 4**). The bandgap evolution for the series of multilayer perovskite compounds under study, along with the PropA and BA series, is shown **Figure 6B**, where the increase of *n* leads to lower bandgaps, ranging from 2.22 eV – 1.90 eV for *n*=2-4 respectively. The PL spectra of the studied crystals include an additional, broad emission peak at lower energy, as seen in **Figure 6E.** The coexistence of narrow- and broadband emission has been studied in n=1 lead halide perovskites[109-110] but to our knowledge, there has not been thorough investigation on the study of broadband emission in in bulk, thick-layer ($n \geq 2$) lead iodide perovskites. This broadband emission in the visible region is thoroughly studied in the *Charge Carrier Dynamics* section below.

Since the bulk perovskites in this study are candidates as light absorbing layers in solar cell devices, photoemission yield spectroscopy in air (PYSA) was utilized to measure the work function of the materials.[111-113] The position of the valence band maxima (VBM) was determined through the PYSA measurements, while the conduction band minimum (CBM) was determined by subtracting the corresponding band gap values (based on the absorption edge) from the measured VBM energies. The PYSA of the *n*=3 and *n*=4 novel 2D perovskite materials were collected: $(AA)_2(MA)_2Pb_3I_{10}$, $(IdPA)_2(MA)_2Pb_3I_{10}$, $(AA)_2(MA)_3Pb_4I_{13}$ and $(IdPA)_2(MA)_3Pb_4I_{13}$, alongside the reference 2D perovskites $(BA)_2(MA)_2Pb_3I_{10}$ and $(BA)_2(MA)_3Pb_4I_{13}$, and 3D $MAPbI_3$ (**Figure 7**). In the comparison of the *n*=3 analogues, the VBM of $(IdPA)_2(MA)_2Pb_3I_{10}$ (5.55 eV) and $(AA)_2(MA)_2Pb_3I_{10}$ (5.56 eV) are close in value, while $(BA)_2(MA)_2Pb_3I_{10}$ (5.37 eV) is smaller (**Figure 7**). In the comparison of the *n*=4 analogues, the VBM is similar in value for all three compounds: $(AA)_2(MA)_3Pb_4I_{13}$ (5.41 eV), $(IdPA)_2(MA)_3Pb_4I_{13}$ (5.42 eV), and $(BA)_2(MA)_3Pb_4I_{13}$ (5.43 eV) (**Figure 7**). Crystalline powder of $MAPbI_3$ was measured with a VBM of 5.44 eV, matching to reported VBM value of 5.43−5.46 eV.[114-115]

Electronic Structure Calculations and Dielectric Properties:

We use density functional theory (DFT) based calculations to inspect the electronic structure of the layered perovskite $(AA)_2(MA)_2Pb_3I_{10}$ and the series $(IdPA)_2(MA)_{n-1}Pb_nI_{3n+1}$. All compounds exhibit typical band structures (**Figure S12**) with direct bandgaps either at Γ ($(IdPA)_2(MA)_{n-1}Pb_nI_{3n+1}$ for *n*=1,2 and $(AA)_2(MA)_2Pb_3I_{10}$) or Y for $(IdPA)_2(MA)_2Pb_3I_{10}$, as well as great dispersions in the directions corresponding to the plane of the perovskite layers and nearly no dispersion in the stacking direction. When going from *n*=1 to *n*=3 in the IdPA series, one can observe the expected electronic band gap

reduction (from 1.55 to 1.14 eV at the chosen level of theory, **Figure S13**) as well the apparition of sub-bands that mark the decrease of quantum confinement for increasing values of *n*. As observed experimentally, the bandgap of the $(AA)_2(MA)_2Pb_3I_{10}$ structure is slightly smaller than the one of the $(IdPA)_2(MA)_2Pb_3I_{10}$ compound. The band structures of $(AA)_2(MA)_2Pb_3I_{10}$ and $(IdPA)_2(MA)_2Pb_3I_{10}$ are very similar (**Figure 8A** and **8B)**, underlying the small electronic influence of spacer cation near the band gap. The similarities extend to other electronic properties, since both layered perovskites also present very close low in-plane electron and hole effective masses (**Figure S14**) around $0.04.m_0$ and $-0.08.m_0$, respectively. Following the *n*=1-3 IdPA series, we observe that the computed in-plane effective masses tend to decrease with increasing values of *n*, which can be traced back to the bandgap reduction.

Layered halide perovskites are not only solution-processed natural quantum wells, they are also dielectric quantum wells, due to the contrast between the dielectric constant of the perovskite layers and that of the organic cation layers. This cannot be described when computing the standard bulk high-frequency dielectric response (ε_∞) for the unit cell that provides an average of both moieties' contributions. Instead, we propose to discuss the evolution of ε_∞ along z following a recipe designed for nanoscale slabs and composite systems. [28, 116] Profiles of the high-frequency dielectric constant along the stacking axis of the *n*=1-3 for the IdPA series and AA structures are shown in **Figure 9** and **Figure S15**. In addition, the profile of the $(BA)_2(MA)_2Pb_3I_{10}$ structure with BA as a spacer is given for comparison (**Figure 9**).[117] **Figure 9** shows the expected shape of such a profile for layered halide perovskites with low values for the region occupied by the organic cations with ε_∞ ~1.9, while the *n*=3 inorganic perovskite slab reaches ε_∞ ~ 5.3. The same value is found for the *n*=3 structures with AA or IdPA as spacers. This value indicates an already reduced dielectric confinement for the perovskite layer. Indeed, the profiles $\varepsilon_\infty(z)$ of the *n*=1-3 IdPA series (**Figure S15**) display an increase from the contribution of the perovskite layer, ranging from $\varepsilon_\infty(z)$ = 4.4 for *n*=1, $\varepsilon_\infty(z)$ = 4.8 for *n*=2 to $\varepsilon_\infty(z)$ = 5.3 for *n*=3, a contribution that would eventually reaches the dielectric constant of bulk $MAPbI_3$.[107] The comparison between the *n*=3 structures: $(IdPA)_2(MA)_2Pb_3I_{10}$, $(AA)_2(MA)_2Pb_3I_{10}$ and $(BA)_2(MA)_2Pb_3I_{10}$ show the much greater contribution in the barrier for IdPA-based 2D series due to the iodine atom found in the organic cation (**Figure 9A**). The large contributions of iodine atoms to $\varepsilon_\infty(z)$ in the barrier was also reported in a n=1 compound to be at the origin of an experimental strong reduction of the exciton binding energy and oscillator strength.[88] AA and BA have closer constants. The one computed for AA depends on the orientation of the double bound with respect to the stacking direction (**Figure S16**). In our static picture,

the contribution of the unsaturated bound is negligible. Rotations of the AA cations probably delivers an average constant closer to the optimal value obtained leading to a greater screening for AA than for BA.

Charge Carrier Dynamics:

Transient absorption (TA) spectra were measured on the newly synthesized AA/IdPA crystal series to study how the nature of the organic spacer affect the excited-state dynamics of thick-layer lead halide perovskites. In the *Description of Crystal Structures* section above, we show that the inclusion of the unsaturated C=C bond and iodine atoms in the organic layers have different impact on the overall lattice structure. The double bond, due to its shorter length greatly reduces the interlayer distance and induces the zero-offset stacking geometry. The iodine atom, because of its polarizable nature and the large steric hinderance it imposes, induces larger distortion within the Pb-I-Pb angles of the inorganic layer. We acquired TA spectra on exfoliated single crystals after pumping the sample at 2.41 eV (0.36 eV above the bandgap) with a broadband probe from 1.5 to 2.4 eV. These spectra contain both positive excited state absorption (ESA, blue) and negative ground state bleaches (red). The ESA features are similar among all four compounds studied [$(AA)_2(MA)_2Pb_3I_{10}$), [$(AA)_x(IdPA)_{1-x}]_2MA_2Pb_3I_{10}$, $(IdPA)_2(MA)_2Pb_3I_{10}$ and $(BA)_2(MA)_2Pb_3I_{10}$)], which have been attributed previously to intraband absorptions of carriers at and above band-edge carriers. [118-121] Here we focus on the energies and dynamics of the negative bleaching signals, which reflect the changing populations of states with energies at and below the bandgap.

Figure 10 (left two columns) shows that the bandgap bleach features peak at 2.05 eV for all four samples, consistent with the previously reported value for *n*=3 perovskites[122] and the ground state absorption spectra in **Figure 10.** The most distinct difference between $(IdPA)_2(MA)_2Pb_3I_{10}$ (**Figure 10A**) and $(AA)_2(MA)_2Pb_3I_{10}$ (**Figure 10C**) with energies lower than the bandgap. TA spectra on $[(AA)_x(IdPA)_{1-x}]_2MA_2Pb_3I_{10}$ (**Figure 10 B**) and $(BA)_2(MA)_2Pb_3I_{10}$ (**Figure 10D**) crystals are taken under the same condition. The relative intensity of the sub-bandgap peak at 1.94 eV (0.11 eV below Eg, marked using orange lines, referred to as '*ladder state*' below) compared to the bandgap peak is 45% of the intensity of the bandgap peak for $(IdPA)_2(MA)_2Pb_3I_{10}$, 37% for $[(AA)_x(IdPA)_{1-x}]_2MA_2Pb_3I_{10}$, 16% for $(AA)_2(MA)_2Pb_3I_{10}$ and 5% for $(BA)_2(MA)_2Pb_3I_{10}$. The relative intensity of the peak at 1.73 eV (0.32 eV below Eg, marked using yellow line, referred to as '*sink state'* below) is 36% of the intensity of the bandgap peak for $(IdPA)_2(MA)_2Pb_3I_{10}$, 15% for $[(AA)_x(IdPA)_{1-x}]_2MA_2Pb_3I_{10}$ and 0% for both $(AA)_2(MA)_2Pb_3I_{10}$ and $(BA)_2(MA)_2Pb_3I_{10}$. These relative intensities indicate that the formation of the

sink state at 1.73 eV is clearly related to the IdPA spacer added into the perovskite lattice, while the formation of the ladder state is a combined effort of both the AA and IdPA cations.

Figure 10 (right column) shows the normalized intensity of the bleaching signals as a function of delay time at the three key energy levels (bandgap, ladder, and sink, notions explained above). Multi-exponential fits are applied to extract the recombination lifetime, which are 17.5 ps for $(IdPA)_2(MA)_2Pb_3I_{10}$, 20.4 ps for $[(AA)_x(IdPA)_{1-x}]_2MA_2Pb_3I_{10}$, 75.4 ps for $(AA)_2(MA)_2Pb_3I_{10}$ and 77.5 ps for $(BA)_2(MA)_2Pb_3I_{10}$ (also marked near the curves in **Figure 10**). The dynamics for the crystal samples containing the IdPA cation are similar in terms of the recombination lifetimes ($(IdPA)_2(MA)_2Pb_3I_{10}$: 17.5 ps vs. $[(AA)_x(IdPA)_{1-x}]_2MA_2Pb_3I_{10}$: 20.4 ps) and the direction of energy flow among states (bandgap → ladder → sink). It is worth noting that the sink states have a lifetime of ~100-ps, which is even longer than the bandgap recombination lifetime of $(BA)_2(MA)_2Pb_3I_{10}$ crystals (77.5 ps) with no below-bandgap trap. This result indicates the decoupling of electron and hole within the sink states.

To better compare the bandgap recombination dynamics of the four studied crystals and the impact of the different spacer cations on the crystal structure, we plot all of the kinetic traces acquired at the bandgap energy in **Figure 11A**. The two traces for the crystals containing IdPA (blue) decay quickly after the initial rise. The trace for $(BA)_2(MA)_2Pb_3I_{10}$ (black) plateaus at 1 ps. The grey trace belonging to $(AA)_2(MA)_2Pb_3I_{10}$ crystals shows two-stage dynamics. It largely resembles the $(IdPA)_2(MA)_2Pb_3I_{10}$ dynamics at early time (<2 ps), but the decay slows down and starts to resemble the $(BA)_2(MA)_2Pb_3I_{10}$ trace after 20 ps. We hypothesize that the different behaviors are related to the different energetic depths of the trap states within the bandgap (ladder: shallow, 0.11 eV below Eg; sink: deep, 0.32 eV below Eg). When the sink state is present, which is the case of $(IdPA)_2(MA)_2Pb_3I_{10}$ and $[(AA)_x(IdPA)_{1-x}]_2MA_2Pb_3I_{10}$ crystals, carriers were quickly drained by the ladder state and then fed to the sink state to recombine. For $(AA)_2(MA)_2Pb_3I_{10}$, the carriers at bandgap were drained quickly as well by the ladder state, and that is why its bandgap signal does not plateau like that of $(BA)_2(MA)_2Pb_3I_{10}$, but without the sink state, the shallow ladder states quickly saturated so the long-term dynamics still resemble those of $(BA)_2(MA)_2Pb_3I_{10}$. The implication of these results is that these defect states could contribute to photovoltage losses on the picosecond timescale in solar cell devices.

The origin of the deep sink state can be further related to lattice distortions caused by the IdPA cation as is shown in **Figure 11B**. The recombination speed of the band-edge carriers, and the degree of lattice distortion, represented by the bond angle of the average equatorial Pb-I-Pb angle, are plotted as

functions of IdPA concentration. A negative correlation between the recombination speed and the bond angle can be easily observed. The biggest change of the two parameters both show up when the amount of IdPA change from 0% for $(AA)_2(MA)_2Pb_3I_{10}$ to 50% $[(AA)_x(IdPA)_{1-x}]_2MA_2Pb_3I_{10}$. The inclusion of the AA spacer, which causes a great change in the stacking geometry, does not seem to have much influence on the recombination process. We may now draw the conclusion that there exist positive correlations between the increased amount of the of IdPA spacer, length of the band-edge recombination lifetime, and the severity of lattice distortion (represented by decreased Pb-I-Pb angle).

The nature of the trap states created by AA and IdPA cations is worth further exploration. The impact of the addition of iodine atoms between the organic layers cannot be neglected. The shallow ladder state could be explained by either a defect state like iodine interstitials [123-125] or a new phonon-assisted recombination pathway.[126] The formation mechanism of the deep sink state may be quite unique, considering its unusual behavior of retaining the carriers longer compared to the band-edge states. One possible explanation is that a "new bandgap" was created by the defect states like Pb vacancies, and then the photogenerated electrons and holes were delocalized and spatially separated in the presence of Pb vacancies, leading to a suppressed radiative charge recombination, as was hypothesized for the BA-based perovskites[127] . The related defect might not be a lead vacancy, since the IdPA spacer with an additional iodine atom was involved, but the recombination suppression mechanism should be similar. A better hypothesis could be developed if the actual form of the charged species were known, but this is far beyond the scope of the current paper. Further research conducted with half-cell and mid-bandgap excitation could pursuit to achieve a more thorough answer.

Conclusions:

Understanding how to engineer the organic layers, which regulate the synthesis, structural character, electronic and photophysical properties of the resultant structure is pivotal for establishing specific synthetic criterion for the rational design and predictive synthesis of hybrid semiconductors. We demonstrate that the inclusion of (non-optically active) functional groups onto the organic cation chain governs the synthetic preparation, crystal chemistry and recombination dynamics of the resultant thick-layer lead iodide perovskite. The bulk synthesis and crystallographic characterization of three new homologous series of $(AA)_2MA_{n-1}Pb_nI_{3n+1}$ (n=3-4), $[(AA)_x(IdPA)_{1-x}]_2MA_{n-1}Pb_nI_{3n+1}$ and $(IdPA)_2MA_{n-1}Pb_nI_{3n+}1$ (n=1-4) of layered perovskites and perovskite-related compounds is reported. For the first time, thick-layered perovskites ($n\geq3$) consisting of organic molecules with heteroatom-functional groups have

been synthesized in bulk. Developing reactions that leverage the inherent reactivity of functional groups within the organic layers, affords the solid solution of $[(AA)_x(IdPA)_{1-x}]_2MA_{n-1}Pb_nI_{3n+1}$, through in-situ formation. Additionally, the synthetic understanding obtained from this work encourages the development of a universal solution method of layered halide perovskites with non-hydrohalic solvents, while emphasizing the imperative necessity of precise structural characterization of bulk and films of hybrid layered perovskites.

The $(AA)_2MA_{n-1}Pb_nI_{3n+1}$ (n=3-4) series adopts the 2D perovskite structure, where the crystal structure of $(AA)_2MA_2Pb_3I_{10}$ is a unique thick-layer structure type close to the DJ type, with an offset (0, < ½). This is a rare example of a thick-layer (n>1), lead halide perovskite with monoammonium spacer cation that affords a non-RP structure type. Instead of the layered perovskite structure, the targeted synthesis of n<2 in the $(AA)_2MA_{n-1}Pb_nI_{3n+1}$ series, yielded the 2D step-like homologous series of non-perovskites $(AA)_{2m+4}(MA)_{m-2}Pb_{2m+1}I_{7m+4}$. $(IdPA)_2MA_2Pb_3I_{10}$ manifests significantly distorted equatorial Pb-I-Pb angles among known n=3 RP perovskites, due to the greater steric interactions from the iodine atom on the IdPA cation. The strength of the electrostatic interactions induced from the spacer cation demonstrates a competing control between the stacking geometry of the consecutive inorganic layers and the distortion level within the Pb-I-Pb inorganic layers. The band-edge absorption and PL emission of $(AA)_2MA_2Pb_3I_{10}$ is around 2.0 eV, redshifted in comparison to $(IdPA)_2MA_2Pb_3I_{10}$ with band-edge absorption 2.03 eV. The band structures of $(AA)_2(MA)_2Pb_3I_{10}$ and $(IdPA)_2(MA)_2Pb_3I_{10}$ resemble, underlying the small electronic influence of the spacer cation near the band gap. Furthermore, the calculated high-frequency dielectric constant profiles of $(AA)_2MA_2Pb_3I_{10}$, $(IdPA)_2MA_2Pb_3I_{10}$ and $(BA)_2MA_2Pb_3I_{10}$ show a greater dielectric contribution from the IdPA cations, owing to the iodine atom in the organic chain. The AA and BA cations have similar dielectric contributions, dependent on the rotations of the AA cation.

The ultrafast study provides new insight on broad emission in 2D halide perovskite materials. The formation of long-lived trap states with broadband emission in the visible region, can be directly related to nature of the organic cation with different functional groups. The crystal compounds containing the IdPA cation manifest shorter recombination lifetimes (~20 ps) than their analogues $(AA)_2MA_2Pb_3I_{10}$ and $(BA)_2MA_2Pb_3I_{10}$ (~ 75 ps). The longer recombination lifetimes of the $(AA)_2MA_2Pb_3I_{10}$ are consistent with those reported previously for AA perovskite films and devices (~90 ps).[47] The inclusion of the IdPA cation, with a heavy and sterically large iodine atom into the 2D perovskite interlayer space instigates significant lattice distortions and leads to the creation of new, broadband ensembles of states deep into

the bandgap. These deep trap states quickly depopulate the band-edge excitons but overall elongate the lifetimes of photoexcited carriers to up to 100 ps.

Acknowledgements:

This work was supported by the Office of Naval Research, under grant N00014-17-1-2231 (synthesis, structural characterization of materials, M.G.K.). E.S.V. acknowledges the Dr. John N. Nicholson fellowship through Northwestern University. This work was supported by the Northwestern Materials Research Science and Engineering Center (NU-MRSEC, DMR-1720139) (measurement of optical properties). This work made use of the NUANCE Center and IMSERC facilities of Northwestern University, which have received support from the Soft and Hybrid Nanotechnology Experimental (SHyNE) Resource (NSF ECCS-2025633). Q.T. acknowledges support through the startup funds from the Texas A&M Engineering Experiment Station (TEES) and the Texas A&M Triads for Transformation (T3) grant. E.S.V. thanks Dr. Ido Hadar, Dr. Abishek Iyer, Dr. Jennifer Rote and Prof. Regan Thomson for productive discussion.

Associated Content:

Supporting Information

Methods, complementary syntheses, additional structural and characterization data: nanoindentation data, single crystal and powder X-ray diffraction, electronic structure and dielectric calculations, optical data, NMR spectroscopy, SEM and microscope images. This material is available free of charge via the Internet at http://pubs.acs.org.

X-ray crystallographic data for $(AA)_2Pb_2I_7$

X-ray crystallographic data for $(AA)_{12}(MA)_2Pb_9I_{32}$

X-ray crystallographic data for $(AA)_2(MA)_2Pb_3I_{10}$ (n=3)

X-ray crystallographic data for $[(AA)_x(IdPA)_{1-x}]_2PbI_4$ (n=1)

X-ray crystallographic data for $[(AA)_x(IdPA)_{1-x}]_2(MA)Pb_2I_7$ (n=2)

X-ray crystallographic data for $[(AA)_x(IdPA)_{1-x}]_2(MA)_2Pb_3I_{10}$ (n=3)

X-ray crystallographic data for $(IdPA)_6Pb_3I_{12}$

X-ray crystallographic data for $(IdPA)PbI_3$

X-ray crystallographic data for $(IdPA)_2PbI_4$ (n=1)

X-ray crystallographic data for $(IdPA)_2(MA)Pb_2I_7$ (n=2)

X-ray crystallographic data for $(IdPA)_2(MA)_2Pb_3I_{10}$ (n=3)

Author Information:

Corresponding Authors
m-kanatzidis@northwestern.edu

Present address #: I.S.: University of South Florida, Tampa, FL, 33620, U.S.

Notes:

The authors declare no competing financial interest.

References:

1. Kojima, A.; Teshima, K.; Shirai, Y.; Miyasaka, T., Organometal Halide Perovskites as Visible-Light Sensitizers for Photovoltaic Cells. *J. Am. Chem. Soc.* **2009,** *131* (17), 6050-6051.
2. Chung, I.; Lee, B.; He, J.; Chang, R. P. H.; Kanatzidis, M. G., All-solid-state dye-sensitized solar cells with high efficiency. *Nature* **2012,** *485* (7399), 486-489.
3. Kim, H.-S.; Lee, C.-R.; Im, J.-H.; Lee, K.-B.; Moehl, T.; Marchioro, A.; Moon, S.-J.; Humphry-Baker, R.; Yum, J.-H.; Moser, J. E.; Grätzel, M.; Park, N.-G., Lead Iodide Perovskite Sensitized All-Solid-State Submicron Thin Film Mesoscopic Solar Cell with Efficiency Exceeding 9%. *Scientific Reports* **2012,** *2* (1), 591.
4. Lee, M. M.; Teuscher, J.; Miyasaka, T.; Murakami, T. N.; Snaith, H. J., Efficient Hybrid Solar Cells Based on Meso-Superstructured Organometal Halide Perovskites. *Science* **2012,** *338* (6107), 643.
5. Stoumpos, C. C.; Kanatzidis, M. G., Halide Perovskites: Poor Man's High-Performance Semiconductors. *Adv. Mater* **2016,** *28* (28), 5778-5793.
6. Tsai, H.; Nie, W.; Blancon, J.-C.; Stoumpos, C. C.; Asadpour, R.; Harutyunyan, B.; Neukirch, A. J.; Verduzco, R.; Crochet, J. J.; Tretiak, S.; Pedesseau, L.; Even, J.; Alam, M. A.; Gupta, G.; Lou, J.; Ajayan, P. M.; Bedzyk, M. J.; Kanatzidis, M. G.; Mohite, A. D., High-efficiency two-dimensional Ruddlesden–Popper perovskite solar cells. *Nature* **2016,** *536*, 312.
7. Arora, N.; Dar, M. I.; Hinderhofer, A.; Pellet, N.; Schreiber, F.; Zakeeruddin, S. M.; Grätzel, M., Perovskite solar cells with CuSCN hole extraction layers yield stabilized efficiencies greater than 20%. *Science* **2017,** *358* (6364), 768-771.
8. Yang, W. S.; Park, B.-W.; Jung, E. H.; Jeon, N. J.; Kim, Y. C.; Lee, D. U.; Shin, S. S.; Seo, J.; Kim, E. K.; Noh, J. H.; Seok, S. I., Iodide management in formamidinium-lead-halide–based perovskite layers for efficient solar cells. *Science* **2017,** *356* (6345), 1376-1379.
9. Tsai, H.; Asadpour, R.; Blancon, J.-C.; Stoumpos, C. C.; Durand, O.; Strzalka, J. W.; Chen, B.; Verduzco, R.; Ajayan, P. M.; Tretiak, S.; Even, J.; Alam, M. A.; Kanatzidis, M. G.; Nie, W.; Mohite, A. D., Light-induced lattice expansion leads to high-efficiency perovskite solar cells. *Science* **2018,** *360* (6384), 67-70.

10. Cao, Y.; Wang, N.; Tian, H.; Guo, J.; Wei, Y.; Chen, H.; Miao, Y.; Zou, W.; Pan, K.; He, Y.; Cao, H.; Ke, Y.; Xu, M.; Wang, Y.; Yang, M.; Du, K.; Fu, Z.; Kong, D.; Dai, D.; Jin, Y.; Li, G.; Li, H.; Peng, Q.; Wang, J.; Huang, W., Perovskite light-emitting diodes based on spontaneously formed submicrometre-scale structures. *Nature* **2018,** *562* (7726), 249-253.
11. Lin, K.; Xing, J.; Quan, L. N.; de Arquer, F. P. G.; Gong, X.; Lu, J.; Xie, L.; Zhao, W.; Zhang, D.; Yan, C.; Li, W.; Liu, X.; Lu, Y.; Kirman, J.; Sargent, E. H.; Xiong, Q.; Wei, Z., Perovskite light-emitting diodes with external quantum efficiency exceeding 20 per cent. *Nature* **2018,** *562* (7726), 245-248.
12. Sutherland, B. R.; Sargent, E. H., Perovskite photonic sources. *Nat. Photonics* **2016,** *10*, 295.
13. Fang, Y.; Dong, Q.; Shao, Y.; Yuan, Y.; Huang, J., Highly narrowband perovskite single-crystal photodetectors enabled by surface-charge recombination. *Nat. Photonics* **2015,** *9* (10), 679-686.
14. Wei, H.; Fang, Y.; Mulligan, P.; Chuirazzi, W.; Fang, H.-H.; Wang, C.; Ecker, B. R.; Gao, Y.; Loi, M. A.; Cao, L.; Huang, J., Sensitive X-ray detectors made of methylammonium lead tribromide perovskite single crystals. *Nat. Photonics* **2016,** *10* (5), 333-339.
15. Wei, H.; DeSantis, D.; Wei, W.; Deng, Y.; Guo, D.; Savenije, T. J.; Cao, L.; Huang, J., Dopant compensation in alloyed CH3NH3PbBr3−xClx perovskite single crystals for gamma-ray spectroscopy. *Nature Materials* **2017,** *16* (8), 826-833.
16. He, Y.; Ke, W.; Alexander, G. C. B.; McCall, K. M.; Chica, D. G.; Liu, Z.; Hadar, I.; Stoumpos, C. C.; Wessels, B. W.; Kanatzidis, M. G., Resolving the Energy of γ-Ray Photons with MAPbI3 Single Crystals. *ACS Photonics* **2018,** *5* (10), 4132-4138.
17. He, Y.; Matei, L.; Jung, H. J.; McCall, K. M.; Chen, M.; Stoumpos, C. C.; Liu, Z.; Peters, J. A.; Chung, D. Y.; Wessels, B. W.; Wasielewski, M. R.; Dravid, V. P.; Burger, A.; Kanatzidis, M. G., High spectral resolution of gamma-rays at room temperature by perovskite CsPbBr3 single crystals. *Nature Communications* **2018,** *9* (1), 1609.
18. Zhu, H.; Fu, Y.; Meng, F.; Wu, X.; Gong, Z.; Ding, Q.; Gustafsson, M. V.; Trinh, M. T.; Jin, S.; Zhu, X. Y., Lead halide perovskite nanowire lasers with low lasing thresholds and high quality factors. *Nature Materials* **2015,** *14* (6), 636-642.
19. Zhang, H.; Liao, Q.; Wu, Y.; Zhang, Z.; Gao, Q.; Liu, P.; Li, M.; Yao, J.; Fu, H., 2D Ruddlesden–Popper Perovskites Microring Laser Array. *Adv. Mater* **2018,** *30* (15), 1706186.
20. Mączka, M.; Gagor, A.; Zaręba, J. K.; Stefanska, D.; Drozd, M.; Balciunas, S.; Šimėnas, M.; Banys, J.; Sieradzki, A., Three-Dimensional Perovskite Methylhydrazinium Lead Chloride with Two Polar Phases and Unusual Second-Harmonic Generation Bistability above Room Temperature. *Chem. Mater.* **2020,** *32* (9), 4072-4082.
21. Mączka, M. a.; Ptak, M.; Gągor, A.; Stefańska, D.; Zaręba, J. K.; Sieradzki, A., Methylhydrazinium Lead Bromide: Noncentrosymmetric Three-Dimensional Perovskite with Exceptionally Large Framework Distortion and Green Photoluminescence. *Chem. Mater.* **2020,** *32* (4), 1667-1673.
22. Stoumpos, C. C.; Frazer, L.; Clark, D. J.; Kim, Y. S.; Rhim, S. H.; Freeman, A. J.; Ketterson, J. B.; Jang, J. I.; Kanatzidis, M. G., Hybrid Germanium Iodide Perovskite Semiconductors: Active Lone Pairs, Structural Distortions, Direct and Indirect Energy Gaps, and Strong Nonlinear Optical Properties. *J. Am. Chem. Soc.* **2015,** *137* (21), 6804-6819.
23. Dieter, W., CH3NH3PbX3, ein Pb(II)-System mit kubischer Perowskitstruktur / CH3NH3PbX3, a Pb(II)-System with Cubic Perovskite Structure. *Zeitschrift für Naturforschung B* **1978,** *33* (12), 1443-1445.
24. Goldschmidt, V. M., Die Gesetze der Krystallochemie. *Naturwissenschaften* **1926,** *14* (21), 477-485.
25. Hanamura, E.; Nagaosa, N.; Kumagai, M.; Takagahara, T., Quantum wells with enhanced exciton effects and optical non-linearity. *Materials Science and Engineering: B* **1988,** *1* (3), 255-258.
26. Muljarov, E. A.; Tikhodeev, S. G.; Gippius, N. A.; Ishihara, T., Excitons in self-organized semiconductor/insulator superlattices: PbI-based perovskite compounds. *Physical Review B* **1995,** *51* (20), 14370-14378.
27. Even, J.; Pedesseau, L.; Katan, C., Analysis of Multivalley and Multibandgap Absorption and Enhancement of Free Carriers Related to Exciton Screening in Hybrid Perovskites. *The Journal of Physical Chemistry C* **2014,** *118* (22), 11566-11572.

28. Even, J.; Pedesseau, L.; Katan, C., Understanding Quantum Confinement of Charge Carriers in Layered 2D Hybrid Perovskites. *ChemPhysChem* **2014,** *15* (17), 3733-3741.
29. Katan, C.; Mercier, N.; Even, J., Quantum and Dielectric Confinement Effects in Lower-Dimensional Hybrid Perovskite Semiconductors. *Chem. Rev.* **2019,** *119* (5), 3140-3192.
30. Blancon, J.-C.; Even, J.; Stoumpos, C. C.; Kanatzidis, M. G.; Mohite, A. D., Semiconductor physics of organic–inorganic 2D halide perovskites. *Nat. Nanotechnol.* **2020,** *15* (12), 969-985.
31. Stoumpos, C. C.; Cao, D. H.; Clark, D. J.; Young, J.; Rondinelli, J. M.; Jang, J. I.; Hupp, J. T.; Kanatzidis, M. G., Ruddlesden–Popper Hybrid Lead Iodide Perovskite 2D Homologous Semiconductors. *Chem. Mater.* **2016,** *28* (8), 2852-2867.
32. Mitzi, D. B.; Feild, C. A.; Harrison, W. T. A.; Guloy, A. M., Conducting tin halides with a layered organic-based perovskite structure. *Nature* **1994,** *369* (6480), 467-469.
33. Li, X.; Hoffman, J. M.; Kanatzidis, M. G., The 2D Halide Perovskite Rulebook: How the Spacer Influences Everything from the Structure to Optoelectronic Device Efficiency. *Chem. Rev.* **2021,** *121* (4), 2230-2291.
34. Saparov, B.; Mitzi, D. B., Organic–Inorganic Perovskites: Structural Versatility for Functional Materials Design. *Chem. Rev.* **2016,** *116* (7), 4558-4596.
35. Zibouche, N.; Islam, M. S., Structure–Electronic Property Relationships of 2D Ruddlesden–Popper Tin- and Lead-based Iodide Perovskites. *ACS Appl. Mater. Interfaces* **2020,** *12* (13), 15328-15337.
36. Byun, J.; Cho, H.; Wolf, C.; Jang, M.; Sadhanala, A.; Friend, R. H.; Yang, H.; Lee, T.-W., Efficient Visible Quasi-2D Perovskite Light-Emitting Diodes. *Adv. Mater* **2016,** *28* (34), 7515-7520.
37. Yuan, M.; Quan, L. N.; Comin, R.; Walters, G.; Sabatini, R.; Voznyy, O.; Hoogland, S.; Zhao, Y.; Beauregard, E. M.; Kanjanaboos, P.; Lu, Z.; Kim, D. H.; Sargent, E. H., Perovskite energy funnels for efficient light-emitting diodes. *Nat. Nanotechnol.* **2016,** *11* (10), 872-877.
38. Vasileiadou, E. S.; Wang, B.; Spanopoulos, I.; Hadar, I.; Navrotsky, A.; Kanatzidis, M. G., Insight on the Stability of Thick Layers in 2D Ruddlesden–Popper and Dion–Jacobson Lead Iodide Perovskites. *J. Am. Chem. Soc.* **2021,** *143* (6), 2523-2536.
39. Vasileiadou, E. S.; Hadar, I.; Kepenekian, M.; Even, J.; Tu, Q.; Malliakas, C. D.; Friedrich, D.; Spanopoulos, I.; Hoffman, J. M.; Dravid, V. P.; Kanatzidis, M. G., Shedding Light on the Stability and Structure–Property Relationships of Two-Dimensional Hybrid Lead Bromide Perovskites. *Chem. Mater.* **2021,** *33* (13), 5085-5107.
40. Vasileiadou, E. S.; Kanatzidis, M. G., Structure-Property Relationships and Idiosyncrasies of Bulk, 2D Hybrid Lead Bromide Perovskites. *Israel Journal of Chemistry,* **2021**, *61*, 1-37.
41. Smith, I. C.; Hoke, E. T.; Solis-Ibarra, D.; McGehee, M. D.; Karunadasa, H. I., A Layered Hybrid Perovskite Solar-Cell Absorber with Enhanced Moisture Stability. *Angew. Chem.* **2014,** *53* (42), 11232-11235.
42. Cao, D. H.; Stoumpos, C. C.; Farha, O. K.; Hupp, J. T.; Kanatzidis, M. G., 2D Homologous Perovskites as Light-Absorbing Materials for Solar Cell Applications. *J. Am. Chem. Soc.* **2015,** *137* (24), 7843-7850.
43. Niu, G.; Guo, X.; Wang, L., Review of recent progress in chemical stability of perovskite solar cells. *J. Mater. Chem. A* **2015,** *3* (17), 8970-8980.
44. Quan, L. N.; Yuan, M.; Comin, R.; Voznyy, O.; Beauregard, E. M.; Hoogland, S.; Buin, A.; Kirmani, A. R.; Zhao, K.; Amassian, A.; Kim, D. H.; Sargent, E. H., Ligand-Stabilized Reduced-Dimensionality Perovskites. *J. Am. Chem. Soc.* **2016,** *138* (8), 2649-2655.
45. Zhao, X.; Ng, J. D. A.; Friend, R. H.; Tan, Z.-K., Opportunities and Challenges in Perovskite Light-Emitting Devices. *ACS Photonics* **2018,** *5* (10), 3866-3875.
46. Mao, L.; Stoumpos, C. C.; Kanatzidis, M. G., Two-Dimensional Hybrid Halide Perovskites: Principles and Promises. *J. Am. Chem. Soc.* **2019,** *141* (3), 1171-1190.
47. Proppe, A. H.; Quintero-Bermudez, R.; Tan, H.; Voznyy, O.; Kelley, S. O.; Sargent, E. H., Synthetic Control over Quantum Well Width Distribution and Carrier Migration in Low-Dimensional Perovskite Photovoltaics. *J. Am. Chem. Soc.* **2018,** *140* (8), 2890-2896.
48. Spanopoulos, I.; Ke, W.; Kanatzidis, M. G., In Quest of Environmentally Stable Perovskite Solar Cells: A Perspective. *Helvetica Chimica Acta* **2021,** *104* (1), e2000173.

49. Hoffman, J. M.; Che, X.; Sidhik, S.; Li, X.; Hadar, I.; Blancon, J.-C.; Yamaguchi, H.; Kepenekian, M.; Katan, C.; Even, J.; Stoumpos, C. C.; Mohite, A. D.; Kanatzidis, M. G., From 2D to 1D Electronic Dimensionality in Halide Perovskites with Stepped and Flat Layers Using Propylammonium as a Spacer. *J. Am. Chem. Soc.* **2019,** *141* (27), 10661-10676.
50. Spanopoulos, I.; Hadar, I.; Ke, W.; Tu, Q.; Chen, M.; Tsai, H.; He, Y.; Shekhawat, G.; Dravid, V. P.; Wasielewski, M. R.; Mohite, A. D.; Stoumpos, C. C.; Kanatzidis, M. G., Uniaxial Expansion of the 2D Ruddlesden–Popper Perovskite Family for Improved Environmental Stability. *J. Am. Chem. Soc.* **2019,** *141* (13), 5518-5534.
51. Mao, L.; Ke, W.; Pedesseau, L.; Wu, Y.; Katan, C.; Even, J.; Wasielewski, M. R.; Stoumpos, C. C.; Kanatzidis, M. G., Hybrid Dion–Jacobson 2D Lead Iodide Perovskites. *J. Am. Chem. Soc.* **2018,** *140* (10), 3775-3783.
52. Li, X.; Ke, W.; Traoré, B.; Guo, P.; Hadar, I.; Kepenekian, M.; Even, J.; Katan, C.; Stoumpos, C. C.; Schaller, R. D.; Kanatzidis, M. G., Two-Dimensional Dion–Jacobson Hybrid Lead Iodide Perovskites with Aromatic Diammonium Cations. *J. Am. Chem. Soc.* **2019,** *141* (32), 12880-12890.
53. Soe, C. M. M.; Stoumpos, C. C.; Kepenekian, M.; Traoré, B.; Tsai, H.; Nie, W.; Wang, B.; Katan, C.; Seshadri, R.; Mohite, A. D.; Even, J.; Marks, T. J.; Kanatzidis, M. G., New Type of 2D Perovskites with Alternating Cations in the Interlayer Space, (C(NH2)3)(CH3NH3)nPbnI3n+1: Structure, Properties, and Photovoltaic Performance. *J. Am. Chem. Soc.* **2017,** *139* (45), 16297-16309.
54. Li, X.; Hoffman, J.; Ke, W.; Chen, M.; Tsai, H.; Nie, W.; Mohite, A. D.; Kepenekian, M.; Katan, C.; Even, J.; Wasielewski, M. R.; Stoumpos, C. C.; Kanatzidis, M. G., Two-Dimensional Halide Perovskites Incorporating Straight Chain Symmetric Diammonium Ions, (NH3CmH2mNH3)(CH3NH3)n−1PbnI3n+1 (m = 4–9; n = 1–4). *J. Am. Chem. Soc.* **2018,** *140* (38), 12226-12238.
55. Li, X.; Fu, Y.; Pedesseau, L.; Guo, P.; Cuthriell, S.; Hadar, I.; Even, J.; Katan, C.; Stoumpos, C. C.; Schaller, R. D.; Harel, E.; Kanatzidis, M. G., Negative Pressure Engineering with Large Cage Cations in 2D Halide Perovskites Causes Lattice Softening. *J. Am. Chem. Soc.* **2020,** *142* (26), 11486-11496.
56. Wang, S.; Mitzi, D. B.; Feild, C. A.; Guloy, A., Synthesis and characterization of [NH2C (I): NH2] 3MI5 (M= Sn, Pb): stereochemical activity in divalent tin and lead halides containing Single. ltbbrac. 110. rtbbrac. Perovskite sheets. *J. Am. Chem. Soc.* **1995,** *117* (19), 5297-5302.
57. Mitzi, D. B.; Dimitrakopoulos, C. D.; Kosbar, L. L., Structurally Tailored Organic−Inorganic Perovskites: Optical Properties and Solution-Processed Channel Materials for Thin-Film Transistors. *Chem. Mater.* **2001,** *13* (10), 3728-3740.
58. Zhu, X.-H.; Mercier, N.; Riou, A.; Blanchard, P.; Frère, P., (C4H3SCH2NH3)2(CH3NH3)Pb2I7 : non-centrosymmetrical crystal structure of a bilayer hybrid perovskite. *Chemical Communications* **2002,** (18), 2160-2161.
59. Mercier, N.; Poiroux, S.; Riou, A.; Batail, P., Unique Hydrogen Bonding Correlating with a Reduced Band Gap and Phase Transition in the Hybrid Perovskites (HO(CH2)2NH3)2PbX4 (X = I, Br). *Inorg. Chem.* **2004,** *43* (26), 8361-8366.
60. Mercier, N., (HO2C(CH2)3NH3)2(CH3NH3)Pb2I7: a predicted non-centrosymmetrical structure built up from carboxylic acid supramolecular synthons and bilayer perovskite sheets. *CrystEngComm* **2005,** *7* (70), 429-432.
61. Billing, D. G.; Lemmerer, A., Poly[bis[2-(1-cyclohexenyl)ethylammonium] di-[mu]-iodo-diodoplumbate(II)]. *Acta Crystallographica Section C* **2006,** *62* (7), m269-m271.
62. Sourisseau, S.; Louvain, N.; Bi, W.; Mercier, N.; Rondeau, D.; Boucher, F.; Buzaré, J.-Y.; Legein, C., Reduced Band Gap Hybrid Perovskites Resulting from Combined Hydrogen and Halogen Bonding at the Organic−Inorganic Interface. *Chem. Mater.* **2007,** *19* (3), 600-607.
63. Mercier, N.; Louvain, N.; Bi, W., Structural diversity and retro-crystal engineering analysis of iodometalate hybrids. *CrystEngComm* **2009,** *11* (5), 720-734.
64. Zhou, C.; Chu, Y.; Ma, L.; Zhong, Y.; Wang, C.; Liu, Y.; Zhang, H.; Wang, B.; Feng, X.; Yu, X.; Zhang, X.; Sun, Y.; Li, X.; Zhao, G., Photoluminescence spectral broadening, chirality transfer and amplification of chiral perovskite

materials (R-X-p-mBZA)2PbBr4 (X = H, F, Cl, Br) regulated by van der Waals and halogen atoms interactions. *Physical Chemistry Chemical Physics* **2020,** *22* (30), 17299-17305.
65. Bala, A.; Kumar, V., Effects of Cl and F Substitution in Phenylethylammonium Spacer Cations on Stability, Structure, and Optical Properties of 2D–3D Ruddlesden–Popper Perovskite Layers. *ACS Applied Energy Materials* **2021,** *4* (2), 1860-1867.
66. Daub, M.; Hillebrecht, H., From 1D to 3D: Perovskites within the System HSC(NH2)2I/CH3NH3I/PbI2 with Maintenance of the Cubic Closest Packing. *Inorg. Chem.* **2021,** *60* (5), 3082-3093.

67. Tian, X.; Hu, Z.; Gao, Z.; Zhang, Y.; Li, C.; Qi, H.; liu, x.; Zheng, R.; Xu, J.; Liu, J., Towards Fluorinated Ruddlesden-Popper Perovskites with Enhanced Physical Properties: A Study on (3-FC6H4CH2CH2NH3)2PbI4 Single Crystals. *Materials Chemistry Frontiers* **2021,** *5* (12), 4645-4657.
68. Chakraborty, R.; Sheikh, T.; Nag, A., Iodine–Iodine Interactions Suppressing Phase Transitions of 2D Layered Hybrid (I-(CH2)n-NH3)2PbI4 (n = 2–6) Perovskites. *Chem. Mater.* **2022,** *34* (1), 288-296.
69. Mitzi, D. B.; Chondroudis, K.; Kagan, C. R., Design, Structure, and Optical Properties of Organic−Inorganic Perovskites Containing an Oligothiophene Chromophore. *Inorg. Chem.* **1999,** *38* (26), 6246-6256.
70. Cortecchia, D.; Soci, C.; Cametti, M.; Petrozza, A.; Martí-Rujas, J., Crystal Engineering of a Two-Dimensional Lead-Free Perovskite with Functional Organic Cations by Second-Sphere Coordination. *ChemPlusChem* **2017,** *82* (5), 681-685.
71. Passarelli, J. V.; Fairfield, D. J.; Sather, N. A.; Hendricks, M. P.; Sai, H.; Stern, C. L.; Stupp, S. I., Enhanced Out-of-Plane Conductivity and Photovoltaic Performance in n = 1 Layered Perovskites through Organic Cation Design. *J. Am. Chem. Soc.* **2018,** *140* (23), 7313-7323.
72. Leveillee, J.; Katan, C.; Even, J.; Ghosh, D.; Nie, W.; Mohite, A. D.; Tretiak, S.; Schleife, A.; Neukirch, A. J., Tuning Electronic Structure in Layered Hybrid Perovskites with Organic Spacer Substitution. *Nano Letters* **2019,** *19* (12), 8732-8740.
73. Tieke, B., Chemical Reactions in Perovskite-Type Layer Structures. *Molecular Crystals and Liquid Crystals* **1983,** *93* (1), 119-145.
74. Tieke, B.; Chapuis, G., Solid-state polymerization of butadienes. Crystal structure and solution properties of a stereoregular amphoteric 1,4-trans-polybutadiene. *Journal of Polymer Science: Polymer Chemistry Edition* **1984,** *22* (11), 2895-2921.
75. Tieke, B.; Chapuis, G., Solid State Polymerization of Butadienes in Layer Structures. *Molecular Crystals and Liquid Crystals* **1986,** *137* (1), 101-116.
76. Mitzi, D. B., Templating and structural engineering in organic–inorganic perovskites. *Journal of the Chemical Society, Dalton Transactions* **2001,** (1), 1-12.
77. Sourisseau, S.; Louvain, N.; Bi, W.; Mercier, N.; Rondeau, D.; Buzaré, J.-Y.; Legein, C., Hybrid Perovskite Resulting from the Solid-State Reaction between the Organic Cations and Perovskite Layers of α1-(Br-(CH2)2-NH3)2PbI4. *Inorg. Chem.* **2007,** *46* (15), 6148-6154.
78. Jaffe, A.; Karunadasa, H. I., Lithium Cycling in a Self-Assembled Copper Chloride–Polyether Hybrid Electrode. *Inorg. Chem.* **2014,** *53* (13), 6494-6496.
79. Solis-Ibarra, D.; Karunadasa, H. I., Reversible and Irreversible Chemisorption in Nonporous-Crystalline Hybrids. *Angew. Chem.* **2014,** *53* (4), 1039-1042.
80. Solis-Ibarra, D.; Smith, I. C.; Karunadasa, H. I., Post-synthetic halide conversion and selective halogen capture in hybrid perovskites. *Chem Sci* **2015,** *6* (7), 4054-4059.
81. Yao, K.; Wang, X.; Xu, Y.-x.; Li, F.; Zhou, L., Multilayered Perovskite Materials Based on Polymeric-Ammonium Cations for Stable Large-Area Solar Cell. *Chem. Mater.* **2016,** *28* (9), 3131-3138.
82. Smith, I. C.; Smith, M. D.; Jaffe, A.; Lin, Y.; Karunadasa, H. I., Between the Sheets: Postsynthetic Transformations in Hybrid Perovskites. *Chem. Mater.* **2017,** *29* (5), 1868-1884.

83. Ortiz-Cervantes, C.; Román-Román, P. I.; Vazquez-Chavez, J.; Hernández-Rodríguez, M.; Solis-Ibarra, D., Thousand-fold Conductivity Increase in 2D Perovskites by Polydiacetylene Incorporation and Doping. *Angew. Chem.* **2018,** *57* (42), 13882-13886.
84. Dolzhenko, Y. I.; Inabe, T.; Maruyama, Y., In Situ X-Ray Observation on the Intercalation of Weak Interaction Molecules into Perovskite-Type Layered Crystals (C9H19NH3)2PbI4 and (C10H21NH3)2CdCl4. *Bulletin of the Chemical Society of Japan* **1986,** *59* (2), 563-567.
85. Papavassiliou, G. C.; Koutselas, I. B.; Terzis, A.; Whangbo, M. H., Structural and electronic properties of the natural quantum-well system (C6H5CH2CH2NH3)2SnI4. *Solid State Communications* **1994,** *91* (9), 695-698.
86. Mitzi, D. B.; Medeiros, D. R.; Malenfant, P. R. L., Intercalated Organic−Inorganic Perovskites Stabilized by Fluoroaryl−Aryl Interactions. *Inorg. Chem.* **2002,** *41* (8), 2134-2145.
87. Billing, D. G.; Lemmerer, A., Synthesis, characterization and phase transitions of the inorganic–organic layered perovskite-type hybrids [(CnH2n+1NH3)2PbI4] (n = 12, 14, 16 and 18). *New Journal of Chemistry* **2008,** *32* (10), 1736-1746.
88. Smith, M. D.; Pedesseau, L.; Kepenekian, M.; Smith, I. C.; Katan, C.; Even, J.; Karunadasa, H. I., Decreasing the electronic confinement in layered perovskites through intercalation. *Chem Sci* **2017,** *8* (3), 1960-1968.
89. Kharasch, M. S.; Fuchs, C. F., THE PEROXIDE EFFECT IN THE ADDITION OF HALOGEN ACIDS TO OLEFINS. XXVII. THE ADDITION OF HALOGEN ACIDS TO ALLYLAMINES AND TRIALKYLALLYLAMMONIUM SALTS. *J. Org. Chem.* **1945,** *10* (2), 159-169.
90. Breton, G. W.; Kropp, P. J.; Harvey, R. G., *Hydrogen Iodide*. : In Encyclopedia of Reagents for Organic Synthesis, (Ed.) doi:10.1002/047084289X.rh039, **2001**, 1-3.

91. Beller, M.; Seayad, J.; Tillack, A.; Jiao, H., Catalytic Markovnikov and anti-Markovnikov Functionalization of Alkenes and Alkynes: Recent Developments and Trends. *Angew. Chem.* **2004,** *43* (26), 3368-3398.
92. Zeng, C.; Shen, G.; Yang, F.; Chen, J.; Zhang, X.; Gu, C.; Zhou, Y.; Fan, B., Rhodium-Catalyzed Generation of Anhydrous Hydrogen Iodide: An Effective Method for the Preparation of Iodoalkanes. *Org. Lett.* **2018,** *20* (21), 6859-6862.
93. Chen, W.; Walker, J. C. L.; Oestreich, M., Metal-Free Transfer Hydroiodination of C–C Multiple Bonds. *J. Am. Chem. Soc.* **2019,** *141* (2), 1135-1140.
94. Xiao, J.; Han, L.-B., Ready access to organoiodides: Practical hydroiodination and double-iodination of carbon-carbon unsaturated bonds with I2. *Tetrahedron* **2019,** *75* (25), 3510-3515.
95. The Stereochemistry of Alkene Addition Reactions. https://www.chemistrysteps.com/stereochemistry-alkenes-addition-reactions/, (Accessed 2021-06).
96. Kour, P.; Chenna Reddy, M.; Pal, S.; Sidhik, S.; Das, T.; Pandey, P.; Mukherjee, S. P.; Chakraborty, S.; Mohite, A. D.; Ogale, S., An Organic–Inorganic Perovskitoid with Zwitterion Cysteamine Linker and its Crystal–Crystal Transformation to Ruddlesden-Popper Phase. *Angew. Chem.* **2021,** *60* (34), 18750-18760.
97. Zhang, Y.; Sun, M.; Zhou, N.; Huang, B.; Zhou, H., Electronic Tunability and Mobility Anisotropy of Quasi-2D Perovskite Single Crystals with Varied Spacer Cations. *The Journal of Physical Chemistry Letters* **2020,** *11* (18), 7610-7616.
98. Tu, Q.; Spanopoulos, I.; Hao, S.; Wolverton, C.; Kanatzidis, M. G.; Shekhawat, G. S.; Dravid, V. P., Out-of-Plane Mechanical Properties of 2D Hybrid Organic–Inorganic Perovskites by Nanoindentation. *ACS Appl. Mater. Interfaces* **2018,** *10* (26), 22167-22173.
99. Tu, Q.; Spanopoulos, I.; Vasileiadou, E. S.; Li, X.; Kanatzidis, M. G.; Shekhawat, G. S.; Dravid, V. P., Exploring the Factors Affecting the Mechanical Properties of 2D Hybrid Organic–Inorganic Perovskites. *ACS Applied Materials & Interfaces* **2020,** *12* (18), 20440-20447.
100. Kim, D.; Vasileiadou, E. S.; Spanopoulos, I.; Kanatzidis, M. G.; Tu, Q., In-Plane Mechanical Properties of Two-Dimensional Hybrid Organic–Inorganic Perovskite Nanosheets: Structure–Property Relationships. *ACS Appl. Mater. Interfaces* **2021,** *13* (27), 31642-31649.

101. Tu, Q.; Kim, D.; Shyikh, M.; Kanatzidis, M. G., Mechanics-coupled stability of metal-halide perovskites. *Matter* **2021,** *4* (9), 2765-2809.
102. Tu, Q.; Spanopoulos, I.; Yasaei, P.; Stoumpos, C. C.; Kanatzidis, M. G.; Shekhawat, G. S.; Dravid, V. P., Stretching and Breaking of Ultrathin 2D Hybrid Organic–Inorganic Perovskites. *ACS Nano* **2018,** *12* (10), 10347-10354.
103. Tu, Q.; Spanopoulos, I.; Hao, S.; Wolverton, C.; Kanatzidis, M. G.; Shekhawat, G. S.; Dravid, V. P., Probing Strain-Induced Band Gap Modulation in 2D Hybrid Organic–Inorganic Perovskites. *ACS Energy Lett.* **2019,** *4* (3), 796-802.
104. Tu, Q.; Spanopoulos, I.; Vasileiadou, E. S.; Li, X.; Kanatzidis, M. G.; Shekhawat, G. S.; Dravid, V. P., Exploring the Factors Affecting the Mechanical Properties of 2D Hybrid Organic-Inorganic Perovskites. *ACS Appl Mater Interfaces* **2020,** *12* (18), 20440-20447.
105. Knutson, J. L.; Martin, J. D.; Mitzi, D. B., Tuning the Band Gap in Hybrid Tin Iodide Perovskite Semiconductors Using Structural Templating. *Inorg. Chem.* **2005,** *44* (13), 4699-4705.
106. Katan, C.; Pedesseau, L.; Kepenekian, M.; Rolland, A.; Even, J., Interplay of spin–orbit coupling and lattice distortion in metal substituted 3D tri-chloride hybrid perovskites. *J. Mater. Chem. A* **2015,** *3* (17), 9232-9240.
107. Traore, B.; Pedesseau, L.; Assam, L.; Che, X.; Blancon, J.-C.; Tsai, H.; Nie, W.; Stoumpos, C. C.; Kanatzidis, M. G.; Tretiak, S.; Mohite, A. D.; Even, J.; Kepenekian, M.; Katan, C., Composite Nature of Layered Hybrid Perovskites: Assessment on Quantum and Dielectric Confinements and Band Alignment. *ACS Nano* **2018,** *12* (4), 3321-3332.
108. Gao, L.; Li, X.; Traoré, B.; Zhang, Y.; Fang, J.; Han, Y.; Even, J.; Katan, C.; Zhao, K.; Liu, S.; Kanatzidis, M. G., m-Phenylenediammonium as a New Spacer for Dion–Jacobson Two-Dimensional Perovskites. *J. Am. Chem. Soc.* **2021,** *143* (31), 12063-12073.
109. Yin, J.; Naphade, R.; Gutiérrez Arzaluz, L.; Brédas, J.-L.; Bakr, O. M.; Mohammed, O. F., Modulation of Broadband Emissions in Two-Dimensional ⟨100⟩-Oriented Ruddlesden–Popper Hybrid Perovskites. *ACS Energy Lett.* **2020**, *5* (7), 2149-2155.
110. Koegel, A. A.; Mozur, E. M.; Oswald, I. W. H.; Jalarvo, N. H.; Prisk, T. R.; Tyagi, M.; Neilson, J. R., Correlating Broadband Photoluminescence with Structural Dynamics in Layered Hybrid Halide Perovskites. *J. Am. Chem. Soc.* **2022,** *144* (3), 1313-1322.
111. Harwell, J. R.; Baikie, T. K.; Baikie, I. D.; Payne, J. L.; Ni, C.; Irvine, J. T. S.; Turnbull, G. A.; Samuel, I. D. W., Probing the energy levels of perovskite solar cells via Kelvin probe and UV ambient pressure photoemission spectroscopy. *Physical Chemistry Chemical Physics* **2016,** *18* (29), 19738-19745.
112. Zhang, J.; Chen, R.; Wu, Y.; Shang, M.; Zeng, Z.; Zhang, Y.; Zhu, Y.; Han, L., Extrinsic Movable Ions in MAPbI3 Modulate Energy Band Alignment in Perovskite Solar Cells. *Advanced Energy Materials* **2018,** *8* (5), 1701981.
113. Guerrero, A.; Bou, A.; Matt, G.; Almora, O.; Heumüller, T.; Garcia-Belmonte, G.; Bisquert, J.; Hou, Y.; Brabec, C., Switching Off Hysteresis in Perovskite Solar Cells by Fine-Tuning Energy Levels of Extraction Layers. *Advanced Energy Materials* **2018,** *8* (21), 1703376.
114. Jung, H. S.; Park, N.-G., Perovskite Solar Cells: From Materials to Devices. *Small* **2015,** *11* (1), 10-25.
115. Ryu, S.; Noh, J. H.; Jeon, N. J.; Chan Kim, Y.; Yang, W. S.; Seo, J.; Seok, S. I., Voltage output of efficient perovskite solar cells with high open-circuit voltage and fill factor. *Energy & Environmental Science* **2014,** *7* (8), 2614-2618.
116. Sapori, D.; Kepenekian, M.; Pedesseau, L.; Katan, C.; Even, J., Quantum confinement and dielectric profiles of colloidal nanoplatelets of halide inorganic and hybrid organic–inorganic perovskites. *Nanoscale* **2016,** *8* (12), 6369-6378.
117. Blancon, J. C.; Stier, A. V.; Tsai, H.; Nie, W.; Stoumpos, C. C.; Traoré, B.; Pedesseau, L.; Kepenekian, M.; Katsutani, F.; Noe, G. T.; Kono, J.; Tretiak, S.; Crooker, S. A.; Katan, C.; Kanatzidis, M. G.; Crochet, J. J.; Even, J.; Mohite, A. D., Scaling law for excitons in 2D perovskite quantum wells. *Nature Communications* **2018,** *9* (1), 2254.
118. Wu, X. X.; Trinh, M. T.; Zhu, X. Y., Excitonic Many-Body Interactions in Two-Dimensional Lead Iodide Perovskite Quantum Wells. *Journal of Physical Chemistry C* **2015,** *119* (26), 14714-14721.

119. Yang, Y.; Ostrowski, D. P.; France, R. M.; Zhu, K.; van de Lagemaat, J.; Luther, J. M.; Beard, M. C., Observation of a hot-phonon bottleneck in lead-iodide perovskites. *Nat. Photonics* **2015,** *10* (1), 53-59.
120. Mondal, A.; Aneesh, J.; Ravi, V. K.; Sharma, R.; Mir, W. J.; Beard, M. C.; Nag, A.; Adarsh, K. V., Ultrafast exciton many-body interactions and hot-phonon bottleneck in colloidal cesium lead halide perovskite nanocrystals. *Physical Review B* **2018,** *98* (11), 115418.
121. Fu, Y.; Jiang, X.; Li, X.; Traore, B.; Spanopoulos, I.; Katan, C.; Even, J.; Kanatzidis, M. G.; Harel, E., Cation Engineering in Two-Dimensional Ruddlesden-Popper Lead Iodide Perovskites with Mixed Large A-Site Cations in the Cages. *J. Am. Chem. Soc.* **2020,** *142* (8), 4008-4021.
122. Blancon, J. C.; Tsai, H.; Nie, W.; Stoumpos, C. C.; Pedesseau, L.; Katan, C.; Kepenekian, M.; Soe, C. M. M.; Appavoo, K.; Sfeir, M. Y.; Tretiak, S.; Ajayan, P. M.; Kanatzidis, M. G.; Even, J.; Crochet, J. J.; Mohite, A. D., PEROVSKITE PHYSICS Extremely efficient internal exciton dissociation through edge states in layered 2D perovskites. *Science* **2017,** *355* (6331), 1288-1291.
123. Meggiolaro, D.; Mosconi, E.; De Angelis, F., Mechanism of Reversible Trap Passivation by Molecular Oxygen in Lead-Halide Perovskites. *ACS Energy Lett.* **2017,** *2* (12), 2794-2798.
124. Meggiolaro, D.; Motti, S. G.; Mosconi, E.; Barker, A. J.; Ball, J.; Andrea Riccardo Perini, C.; Deschler, F.; Petrozza, A.; De Angelis, F., Iodine chemistry determines the defect tolerance of lead-halide perovskites. *Energy & Environmental Science* **2018,** *11* (3), 702-713.
125. De Angelis, F.; Petrozza, A., Clues from defect photochemistry. *Nat Mater* **2018,** *17* (5), 383-384.
126. Gong, X.; Voznyy, O.; Jain, A.; Liu, W.; Sabatini, R.; Piontkowski, Z.; Walters, G.; Bappi, G.; Nokhrin, S.; Bushuyev, O.; Yuan, M.; Comin, R.; McCamant, D.; Kelley, S. O.; Sargent, E. H., Electron-phonon interaction in efficient perovskite blue emitters. *Nat Mater* **2018,** *17* (6), 550-556.
127. Gao, Y.; Zhang, M.; Zhang, X.; Lu, G., Decreasing Exciton Binding Energy in Two-Dimensional Halide Perovskites by Lead Vacancies. *J Phys Chem Lett* **2019,** *10* (14), 3820-3827.

Table 1. Summary of Structural and Optical Properties of All Novel Reported Compounds

Compound	*n* member	Space group (SCXRD)	d_{100} spacing	Bandgap (eV)	PL (eV)	Bandgap recombination lifetimes (ps)
$[(AA)_x(ldPA)_{1-x}]_2PbI_4$	$n = 1$	$P2_1/c$	12.7 Å (SCXRD)	2.39	2.35	-
$(ldPA)_2PbI_4$	$n = 1$	$P2_1/c$	14.6 Å (SCXRD)	2.33	2.29	-
$[(AA)_x(ldPA)_{1-x}]_2MAPb_2I_7$	$n = 2$	Cc	19.6 Å (SCXRD)	2.20	2.15	-
$(ldPA)_2MAPb_2I_7$	$n = 2$	$C2/c$	20.3 Å (SCXRD)	2.22	2.19	-
$(AA)_2MA_2Pb_3I_{10}$	$n = 3$	$P2_1/c$	24.2 Å (SCXRD)	2.01	1.99	75.4
$[(AA)_x(ldPA)_{1-x}]_2MA_2Pb_3I_{10}$	$n = 3$	Pc	26.4 Å (SCXRD)	2.02	2.01	20.4
$(ldPA)_2MA_2Pb_3I_{10}$	$n = 3$	$P2_1/c$	26.9 Å (SCXRD)	2.03	2.02	17.5
$(AA)_2MA_3Pb_4I_{13}$	$n = 4$	-	30.5 Å (PXRD)	1.91	1.90	-
$[(AA)_x(ldPA)_{1-x}]_2MA_3Pb_4I_{13}$	$n = 4$	-	32.7 Å (PXRD)	1.94	1.91	-
$(ldPA)_2MA_3Pb_4I_{13}$	$n = 4$	-	33.1 Å (PXRD)	1.99	1.92	-
$(AA)_3Pb_2I_7$	n=1 Corner & face-sharing connectivity	$P2_12_12_1$	-	2.51	-	-
$(AA)_{12}(MA)_2Pb_9I_{32}$	n=2 Corner & face-sharing connectivity	$P\bar{1}$	-	2.44	-	-
$(ldPA)_6Pb_3I_{12}$	0D	$P\bar{1}$	-	2.73	-	-
$(ldPA)PbI_3$	1D	$P2_1/c$	-	2.49	-	-

Table 2. Crystal Data and Structure Refinement for $(AA)_3Pb_2I_7$, $(AA)_{12}(MA)_2Pb_2I_7$ and $(AA)_2(MA)_2Pb_3I_{10}$ (n=3).

	$(AA)_3Pb_2I_7$	$(AA)_{12}(MA)_2Pb_9I_{32}$	$(AA)_2(MA)_2Pb_3I_{10}$ (n=3)
Empirical formula	$C_9H_{24}N_3Pb_2I_7$	$C_{38}H_{108}N_{14}Pb_9I_{32}$	$C_8H_{28}N_4Pb_3I_{10}$
Crystal system	orthorhombic	triclinic	monoclinic
Space group	$P2_12_12_1$	$P\bar{1}$	$P2_1/c$
Crystal Shape and Color	Yellow Needle	Orange Needle	Dark Red Plate
Unit cell dimensions (Å)	a = 8.758 (11)	a = 8.7900(18)	a = 24.1169(9)
	b = 15.172 (2)	b = 18.750(4)	b = 8.9698(2)
	c = 22.349 (3)	c = 22.950(5)	c = 8.8406(2)
	$\alpha = \beta = \gamma = 90°$	$\alpha = 113.67(3)°$ $\beta = 94.65(3)°$ $\gamma = 96.70(3)°$	$\beta = 93.109(2)°$
Volume ($Å^3$)	2969.8 (7)	3406.3(14)	1909.62(9)
Z	4	1	2
Density (calculated, g/cm^3)	3.303	3.244	3.6017
Independent reflections	5828 [R_{int} = 0.0636]	127081 [R_{int} = 0.1950]	3450 [R_{int} = 0.0942]
Completeness to $\theta = 25.242°/25.242°/32.24°$	99.9%	100%	98%
Data k/ restraints / parameters	5829 / 11 / 130	18434 / 37 / 285	3450 / 6 / 82
Goodness-of-fit	1.017	0.795	3.96
Final R indices [$I>2\sigma(I)$]	R_{obs} = 0.0397, wR_{obs} = 0.0939	R_{obs} = 0.0531, wR_{obs} = 0.1281	R_{obs} = 0.0839, wR_{obs} = 0.2054
R indices [all data]	R_{all} = 0.0539, wR_{all} = 0.1006	R_{all} = 0.1767, wR_{all} = 0.1540	R_{all} = 0.0977, wR_{all} = 0.2073

Table 3. Crystal Data and Structure Refinement for $(IdPA)_2MA_{n-1}Pb_nI_{3n+1}$ (n=1-3).

	$(IdPA)_2PbI_4$ (n =1)	$(IdPA)_2(MA)Pb_2I_7$ (n =2)	$(IdPA)_2(MA)_2Pb_3I_{10}$ (n=3)
Empirical formula	$C_6H_{18}N_2PbI_6$	$C_7H_{24}N_3Pb_2I_9$	$C_8H_{30}N_4Pb_3I_{12}$
Crystal system	monoclinic	monoclinic	monoclinic
Space group	$P2_1/c$	$C2/c$	$P2_1/c$
Crystal Shape and Color	Orange Plate	Red plate	Dark Red Plate
Unit cell dimensions (Å)	a = 14.6130(12)	a = 40.690(2)	a = 26.9377(14)
	b = 8.810(8)	b = 8.8397(3)	b = 8.8439(4)
	c = 8.790(3)	c = 8.8425(4))	c = 8.8540(4)
	β = 106.320(12)°	β = 91.656(4)°	β = 98.113(5)°
Volume ($Å^3$)	1086.0(3)	3179.2(3)	2088.22(17)
Z	4	4	2
Density (calculated, g/cm^3)	3.323	3.578	3.700
Independent reflections	1515 [R_{int} = 0.0706]	3623 [R_{int} = 0.0750]	4101 [R_{int} = 0.0840]
Completeness to θ = 29.51°/27.5°/25.242°	100%	100%	99.9%
Data / restraints / parameters	1515 / 6 / 48	3615 / 0 / 97	4101 / 7 / 95
Goodness-of-fit	1.054	1.062	1.029
Final R indices [I>2σ(I)]	R_{obs} = 0.1063, wR_{obs} = 0.3049	R_{obs} = = 0.0788, wR_{obs} = 0.2310	R_{obs} = 0.1052, wR_{obs} = 0.2961
R indices [all data]	R_{all} = 0.1879, wR_{all} = 0.3520	R_{all} = 0.0924, wR_{all} = 0.2420	R_{all} = 0.1130, wR_{all} = 0.3033

Figures:

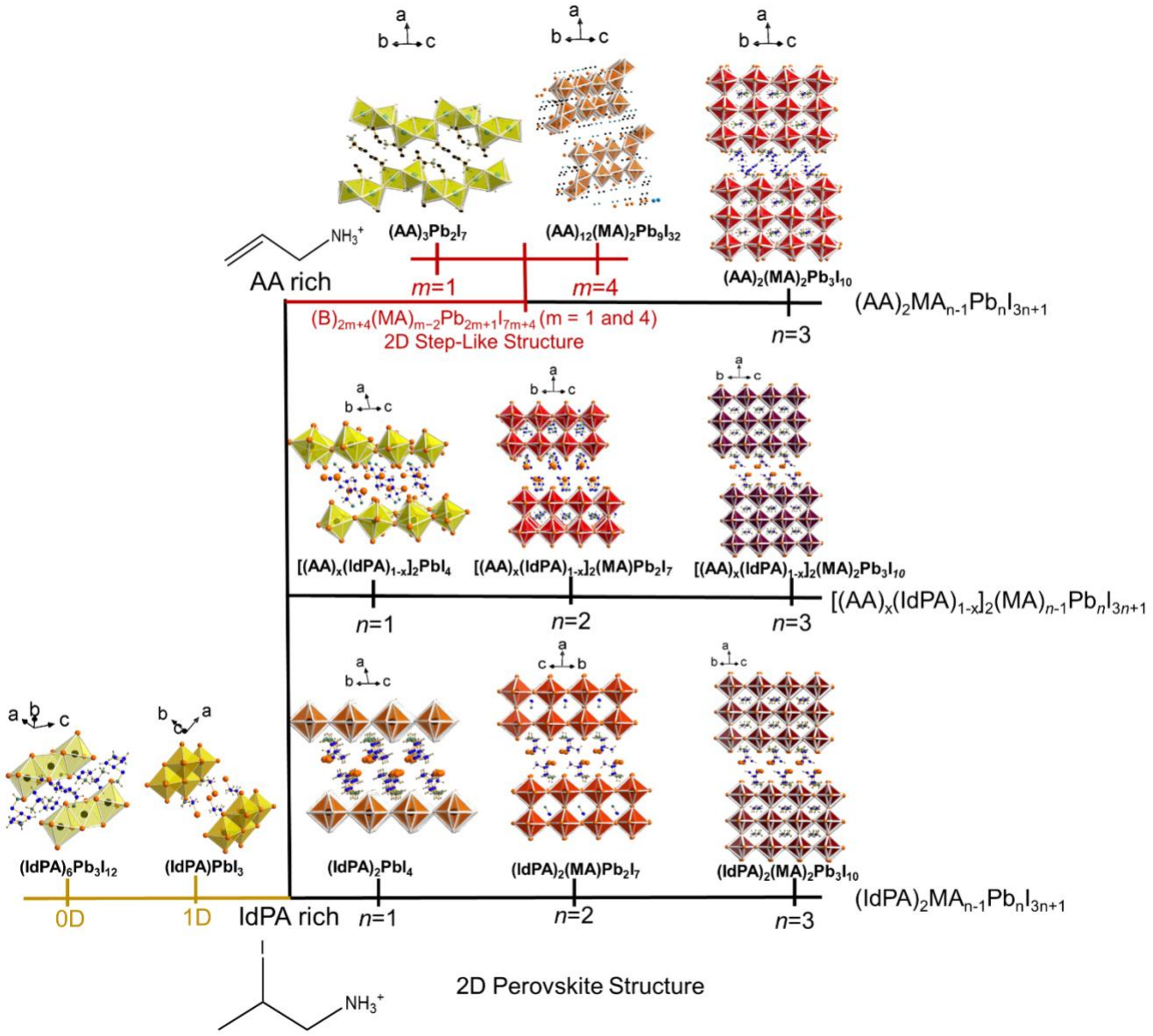

Figure 1. Structural overview of newly reported series of (100) lead iodide perovskites: $(AA)_2MA_{n-1}Pb_nI_{3n+1}$ (n=3-4), $[(AA)_x(IdPA)_{1-x}]_2MA_{n-1}Pb_nI_{3n+1}$ and $(IdPA)_2MA_{n-1}Pb_nI_{3n+}1$ (n=1-4), as well as their perovskite-related substructures: $(AA)_2Pb_2I_7$, $(AA)_{12}(MA)_2Pb_9I_{32}$, $(IdPA)PbI_3$ and $(IdPA)_6Pb_3I_{12}$.

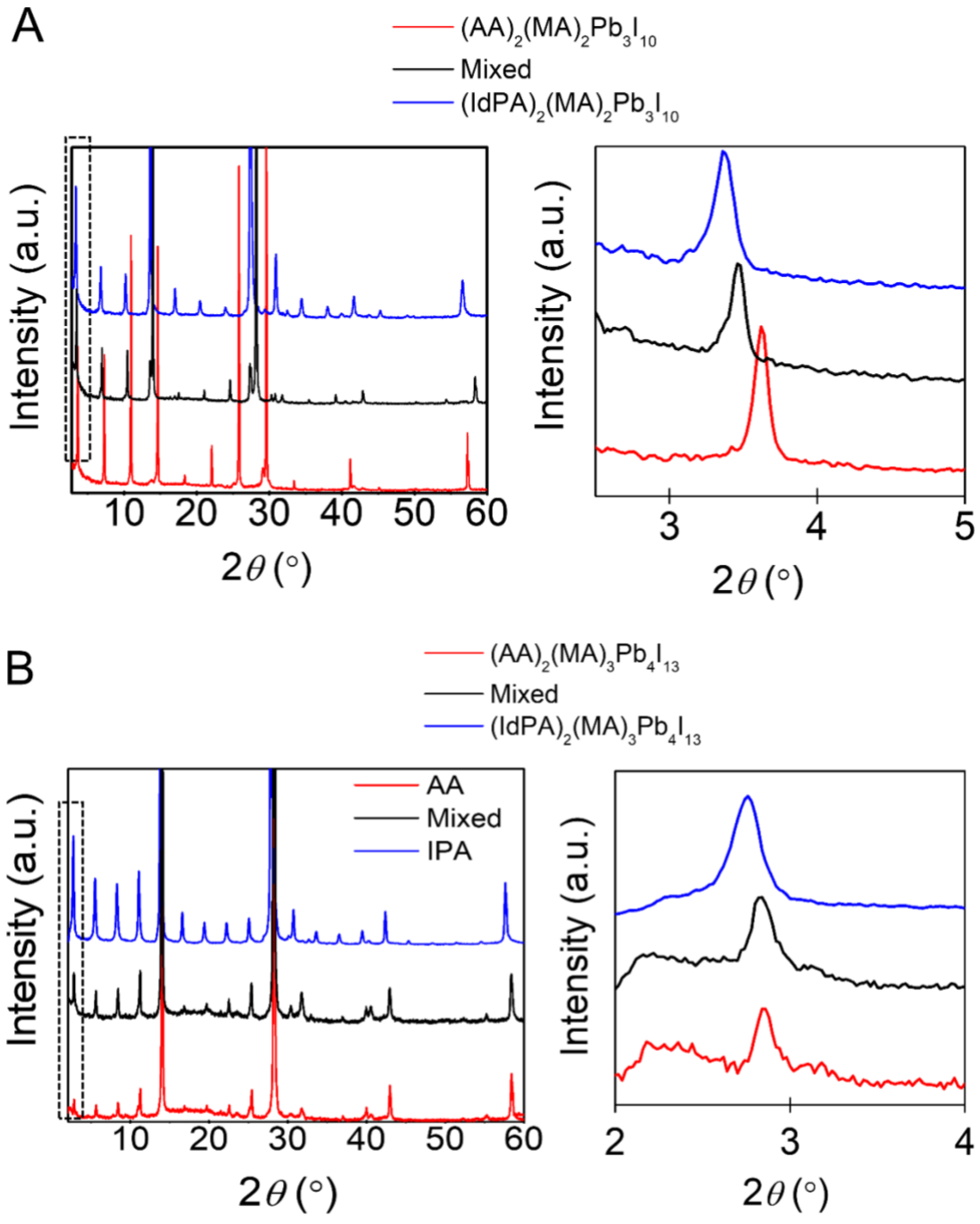
A
(AA)2(MA)2Pb3I10
Mixed
(IdPA)2(MA)2Pb3I10
Intensity (a.u.)
10 20 30 40 50 60
2θ (°)
Intensity (a.u.)
3 4 5
2θ (°)
B
(AA)2(MA)3Pb4I13
Mixed
(IdPA)2(MA)3Pb4I13
AA
Mixed
IPA
Intensity (a.u.)
10 20 30 40 50 60
2θ (°)
Intensity (a.u.)
2 3 4
2θ (°)

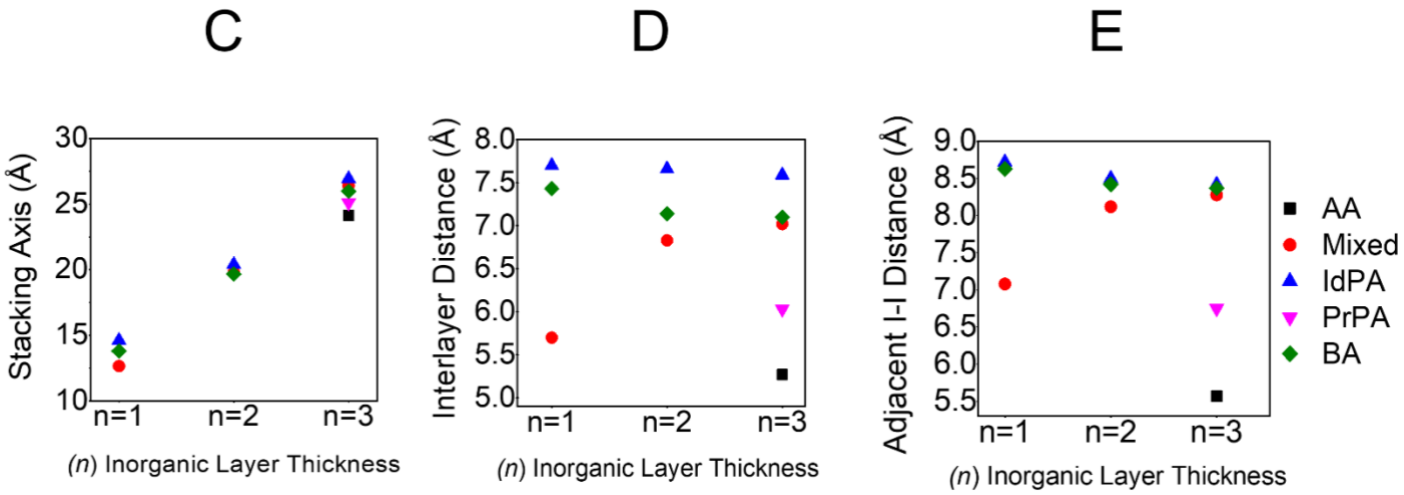

Figure 2. (A) PXRD pattern for *n*=3 compounds $(AA)_2(MA)_2Pb_3I_{10}$, $[(AA)_x(IdPA)_{1-x}]_2(MA)_2Pb_3I_{10}$ and $(IdPA)_2(MA)_2Pb_3I_{10}$ along with the expanded view of the (100) reflections. **(B)** PXRD pattern for *n*=4 compounds $(AA)_2(MA)_3Pb_4I_{13}$, $[(AA)_x(IdPA)_{1-x}]_2(MA)_3Pb_4I_{13}$ and $(IdPA)_2(MA)_3Pb_4I_{13}$ along with the expanded view of the (100) reflections. **(C)** Stacking axis as a function of perovskite layer thickness (*n*), **(D)** Interlayer distance as a function of perovskite layer thickness (*n*), and **(E)** Adjacent I···I distances as a function of perovskite layer thickness (*n*) for the series: $(AA)_2(MA)_{n-1}Pb_nI_{3n+1}$, $[(AA)_x(IdPA)_{1-x}]_2(MA)_{n-1}Pb_nI_{3n+1}$, $(IdPA)_2(MA)_{n-1}Pb_nI_{3n+1}$, $(PrpA)_2(MA)_{n-1}Pb_nI_{3n+1}$ and $(BA)(MA)_{n-1}Pb_nI_{3n+1}$.

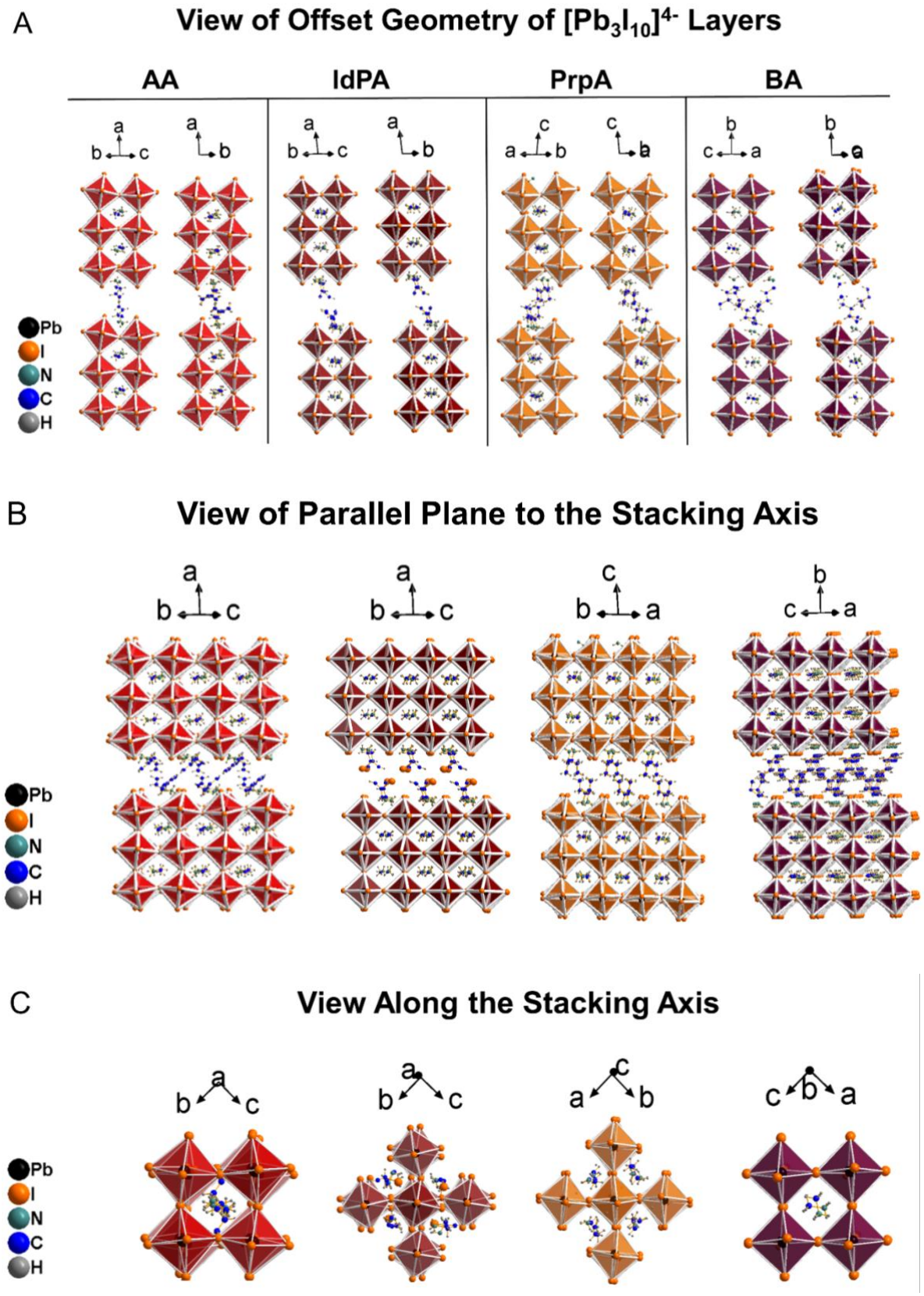
A
View of Offset Geometry of [Pb3I10]4- Layers
AA
IdPA
PrpA
BA
Pb
I
N
C
H
B
View of Parallel Plane to the Stacking Axis
Pb
I
N
C
H
C
View Along the Stacking Axis
Pb
I
N
C
H

Figure 3. (A) Comparative view of the offset geometry in the consecutive $[PbI_6]^{4-}$ layers, (**B**) Comparative view of the parallel plane to the stacking axis, and **(C)** Comparative view along the stacking axis between the (*n*=3) compounds $(AA)_2(MA)_2Pb_3I_{10}$, $(IdPA)_2(MA)_2Pb_3I_{10}$, $(PrpA)_2(MA)_2Pb_3I_{10}$ and $(BA)_2(MA)_2Pb_3I_{10}$.

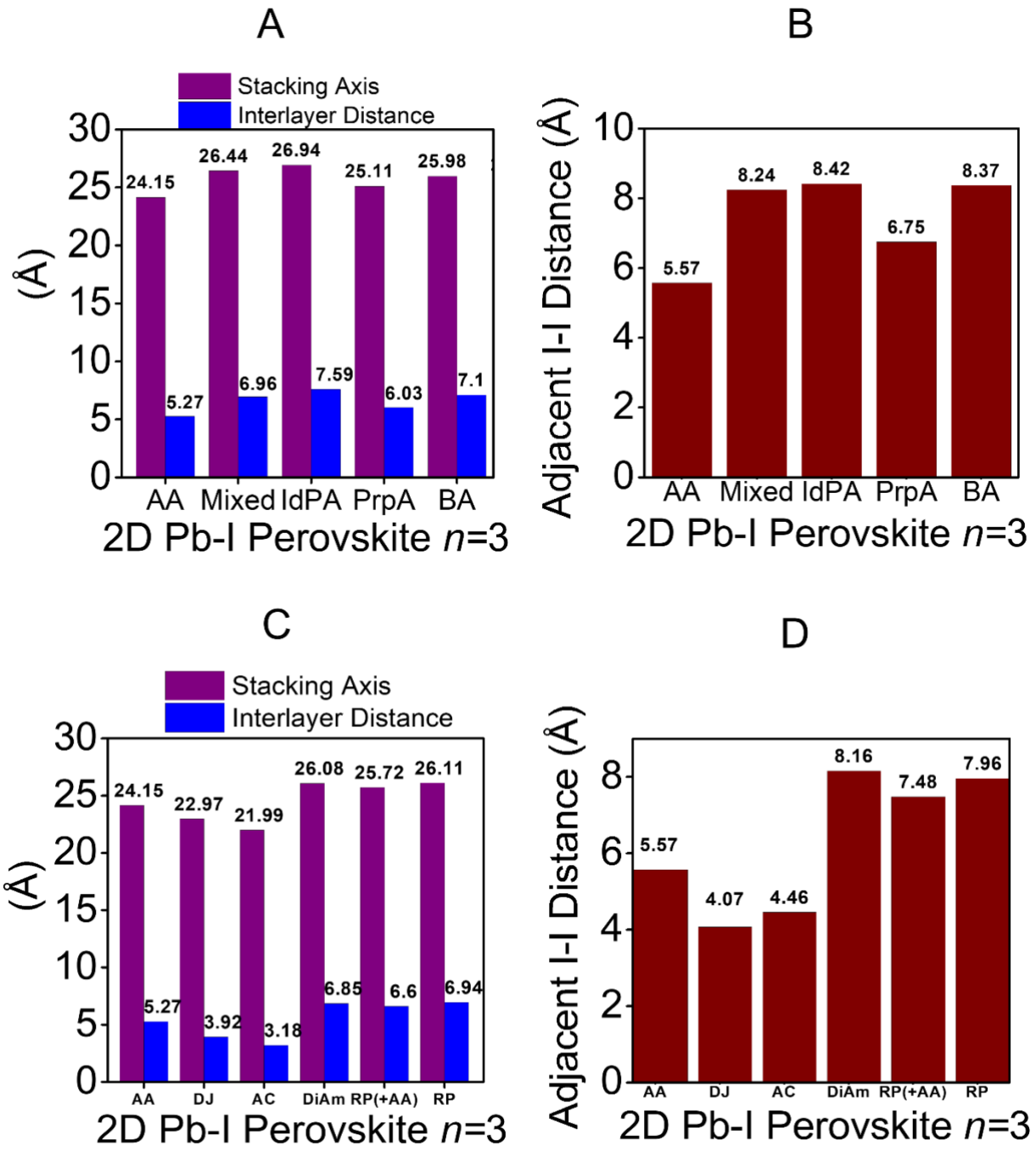

Figure 4. (A) Comparison of the stacking axis and interlayer distance in Å, and **(B)** Comparison of adjacent I···I distances between the (*n*=3) compounds $(AA)_2(MA)_2Pb_3I_{10}$, $[(AA)_x(IdPA)_{1-x}]_2(MA)_2Pb_3I_{10}$, $(IdPA)_2(MA)_2Pb_3I_{10}$, $(PrpA)_2(MA)_2Pb_3I_{10}$ and $(BA)_2(MA)_2Pb_3I_{10}$. **(C)** Comparison of the stacking axis and interlayer distance in Å, and **(D)** Comparison of adjacent I···I distances between the (*n*=3) analogues of the 2D perovskite families of RP, DJ (consisting of the average adjacent I···I distance from the compounds: $(3AMP)MA_2Pb_3I_{10}$, $(4AMP)MA_2Pb_3I_{10}$, $(3AMPY)MA_2Pb_3I_{10}$ and $(4AMPY)MA_2Pb_3I_{10}$), AC (consisting of the compound

(GA)$MA_3Pb_3I_{10}$), DiAm (consisting of the average adjacent I···I distance from the compounds: $(NH_3C_8H_{16}NH_3)(MA)_2Pb_3I_{10}$ and $(NH_3C_9H_{18}NH_3)(MA)_2Pb_3I_{10}$), RP -including $(AA)_2(MA)_2Pb_3I_{10}$ - and the $(AA)_2(MA)_2Pb_3I_{10}$ representative compound.

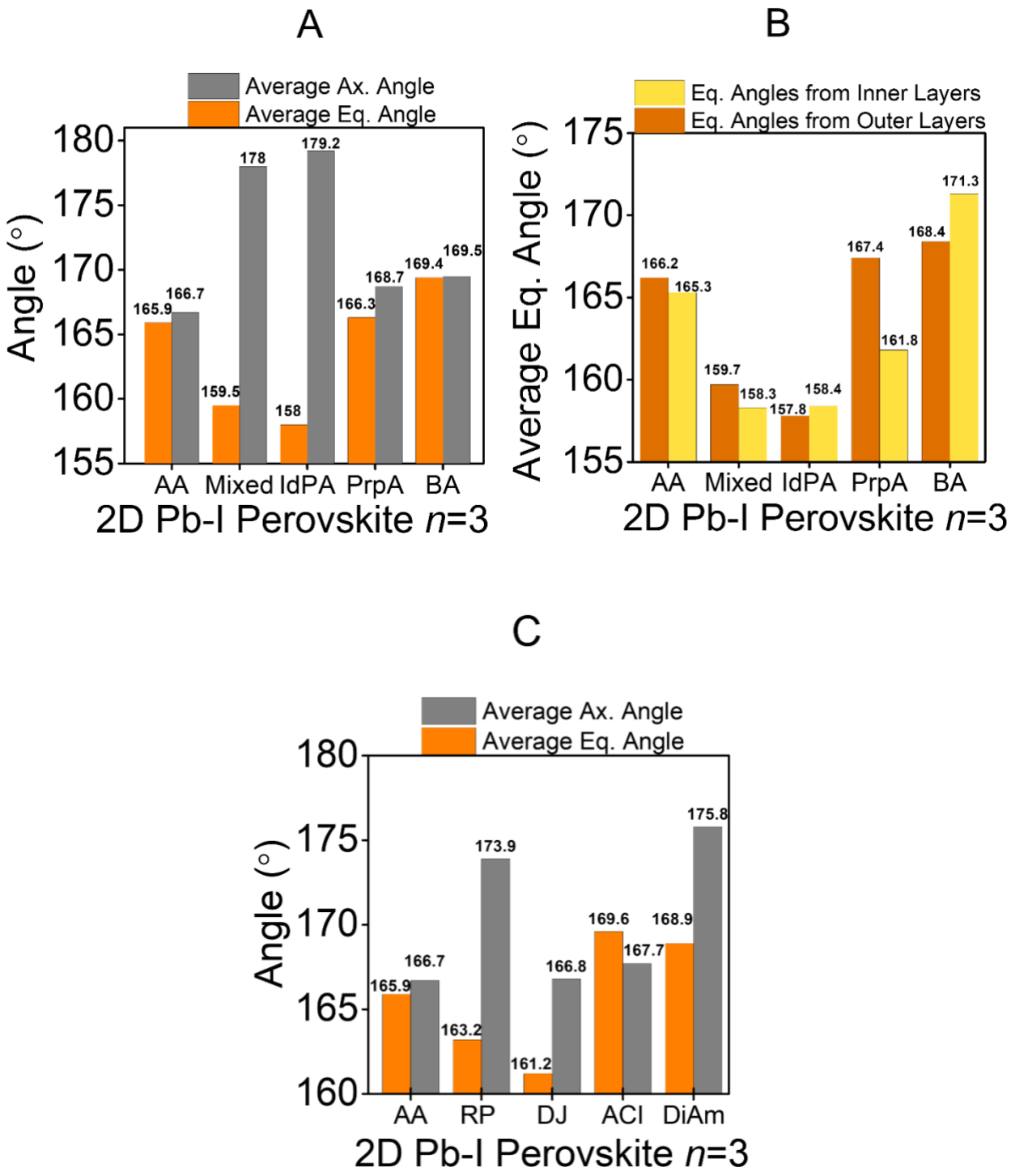

Figure 5. (A) Average axial and equatorial Pb−I−Pb angles of (*n*=3) compounds $(AA)_2(MA)_2Pb_3I_{10}$, $[(AA)_x(IdPA)_{1-x}]_2(MA)_2Pb_3I_{10}$, $(IdPA)_2(MA)_2Pb_3I_{10}$, $(PrpA)_2(MA)_2Pb_3I_{10}$ and $(BA)_2(MA)_2Pb_3I_{10}$. **(B)** Average equatorial Pb−I−Pb angles from the individual inner and outer $[PbI_6]$ layers of the (*n*=3) compounds $(AA)_2(MA)_2Pb_3I_{10}$, $[(AA)_x(IdPA)_{1-x}]_2(MA)_2Pb_3I_{10}$, $(IdPA)_2(MA)_2Pb_3I_{10}$, $(PrpA)_2(MA)_2Pb_3I_{10}$ and

$(BA)_2(MA)_2Pb_3I_{10}$. **(C)** Average axial and equatorial Pb−I−Pb angles of the (*n*=3) analogues of the 2D perovskite families of RP(without AA), DJ (consisting of the compounds: $(3AMP)MA_2Pb_3I_{10}$, $(4AMP)MA_2Pb_3I_{10}$, $(3AMPY)MA_2Pb_3I_{10}$ and $(4AMPY)MA_2Pb_3I_{10}$), AC (consisting of the compound $(GA)MA_3Pb_3I_{10}$), DiAm (consisting of the compounds: $(NH_3C_8H_{16}NH_3)(MA)_2Pb_3I_{10}$ and $(NH_3C_9H_{18}NH_3)(MA)_2Pb_3I_{10}$), and $(AA)_2(MA)_2Pb_3I_{10}$ representative compound.

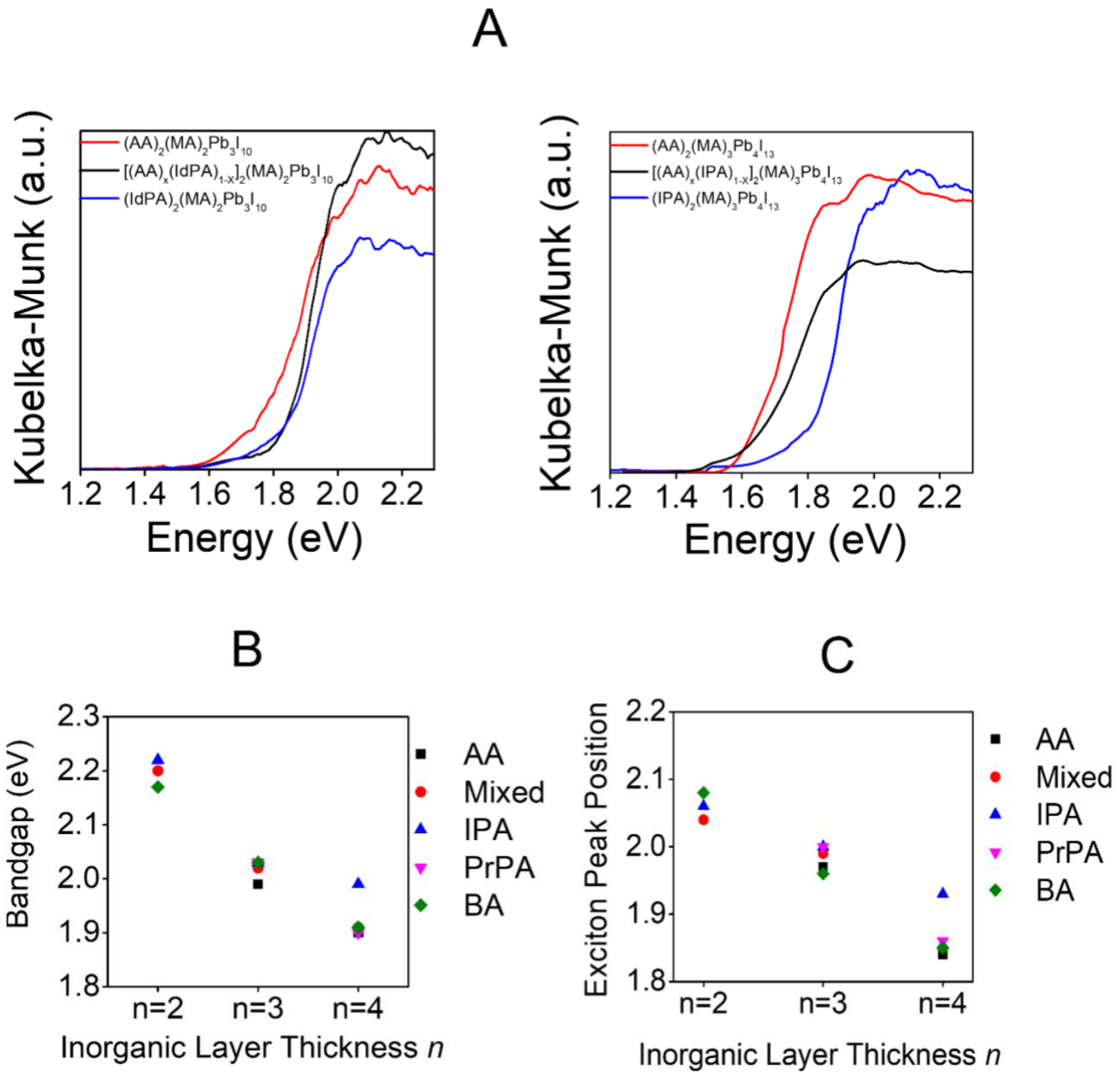

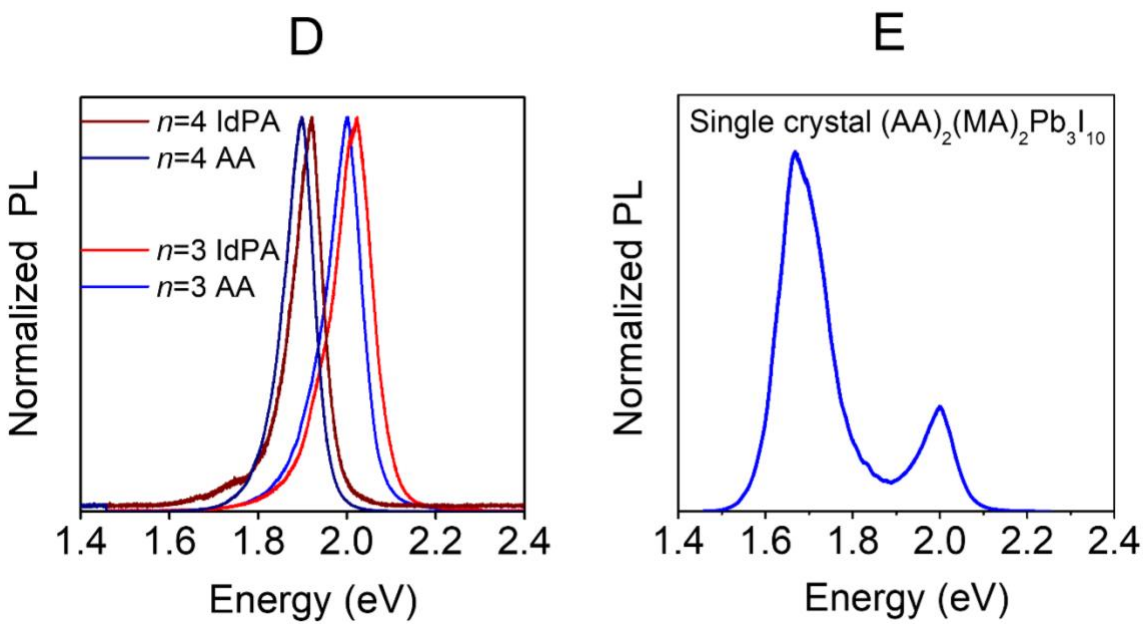

Figure 6. (A) Optical absorption spectra of *n*=3 compounds $(AA)_2(MA)_2Pb_3I_{10}$, $[(AA)_x(IdPA)_{1-x}]_2(MA)_2Pb_3I_{10}$, and $(IdPA)_2(MA)_2Pb_3I_{10}$ and *n*=4 compounds $(AA)_2(MA)_3Pb_4I_{13}$, $[(AA)_x(IdPA)_{1-x}]_2(MA)_3Pb_4I_{13}$ and $(IdPA)_2(MA)_3Pb_4I_{13}$. **(B)** Bandgap and **(C)** exciton peak as a function of perovskite layer thickness (*n*) for the series: $(AA)_2(MA)_{n-1}Pb_nI_{3n+1}$, $[(AA)_x(IdPA)_{1-x}]_2(MA)_{n-1}Pb_nI_{3n+1}$, $(IdPA)_2(MA)_{n-1}Pb_nI_{3n+1}$, $(PrpA)_2(MA)_{n-1}Pb_nI_{3n+1}$ and $(BA)(MA)_{n-1}Pb_nI_{3n+1}$ (*n*=2-4). **(D)** Band-edge emission of $(AA)_2(MA)_2Pb_3I_{10}$, $(IdPA)_2(MA)_2Pb_3I_{10}$, $(AA)_2(MA)_3Pb_4I_{13}$, and $(IdPA)_2(MA)_3Pb_4I_{13}$. **(E)** Observation of broad emission in $(AA)_2(MA)_2Pb_3I_{10}$ crystal.

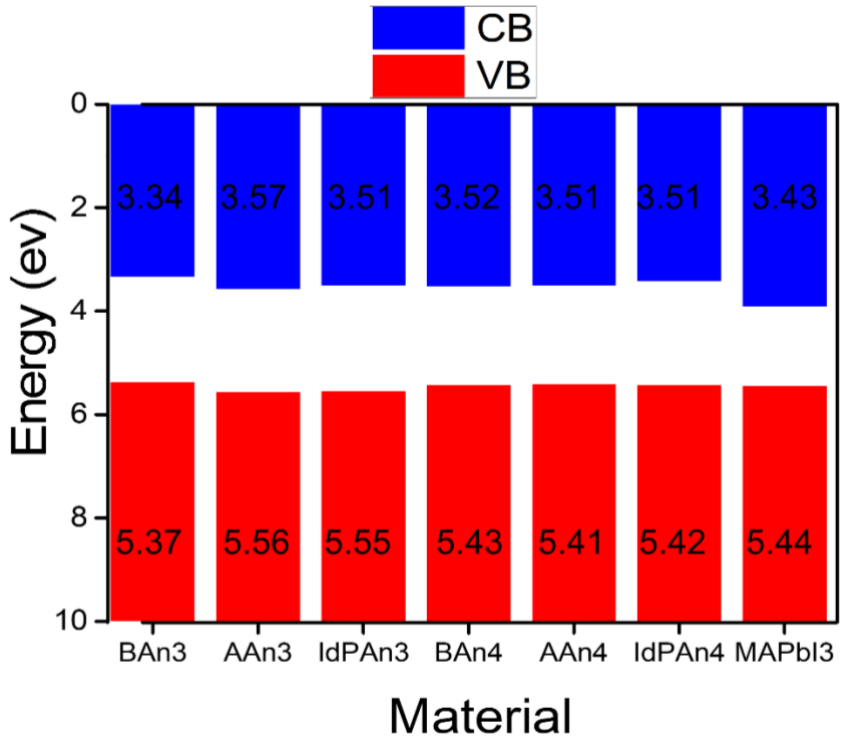

Figure 7. Photoemission Yield Spectroscopy in Air (PYSA) of $(BA)_2(MA)_2Pb_3I_{10}$, $(AA)_2(MA)_2Pb_3I_{10}$, $(IdPA)_2(MA)_2Pb_3I_{10}$, $(BA)_2(MA)_3Pb_4I_{13}$, $(AA)_2(MA)_3Pb_4I_{13}$, $(IdPA)_2(MA)_3Pb_4I_{13}$ and $MAPbI_3$.

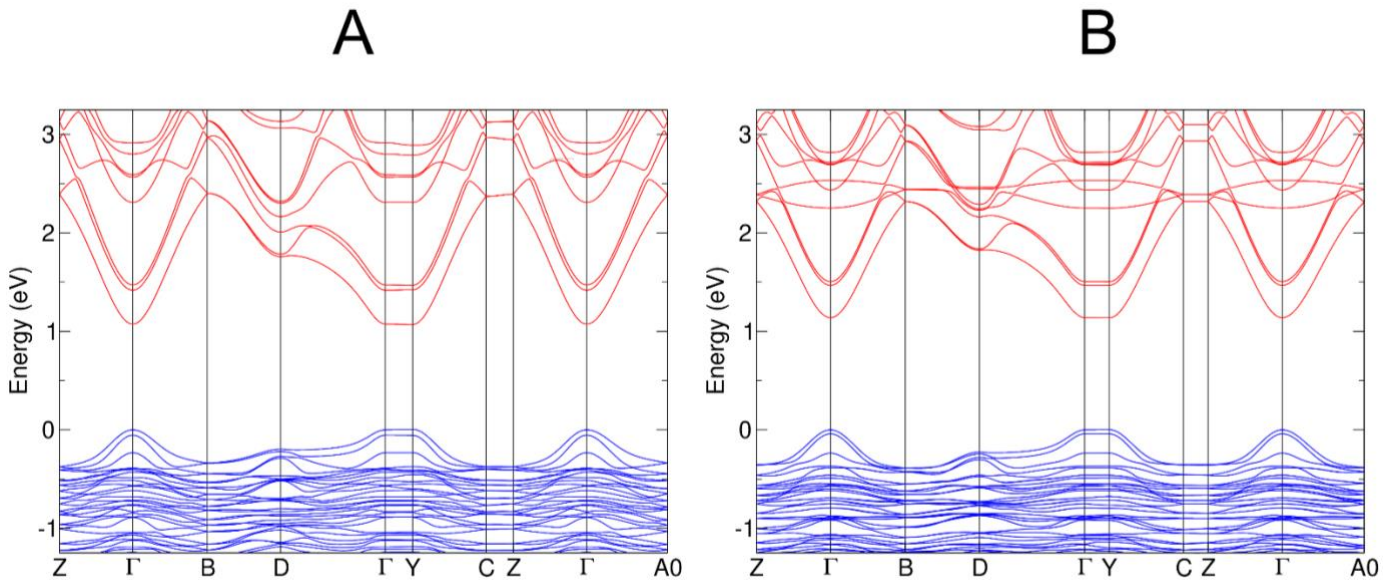

Figure 8. Computed band structures for (**A**) $(AA)_2MA_2Pb_3I_{10}$ and (**B**) $(IdPA)_2MA_2Pb_3I_{10}$.

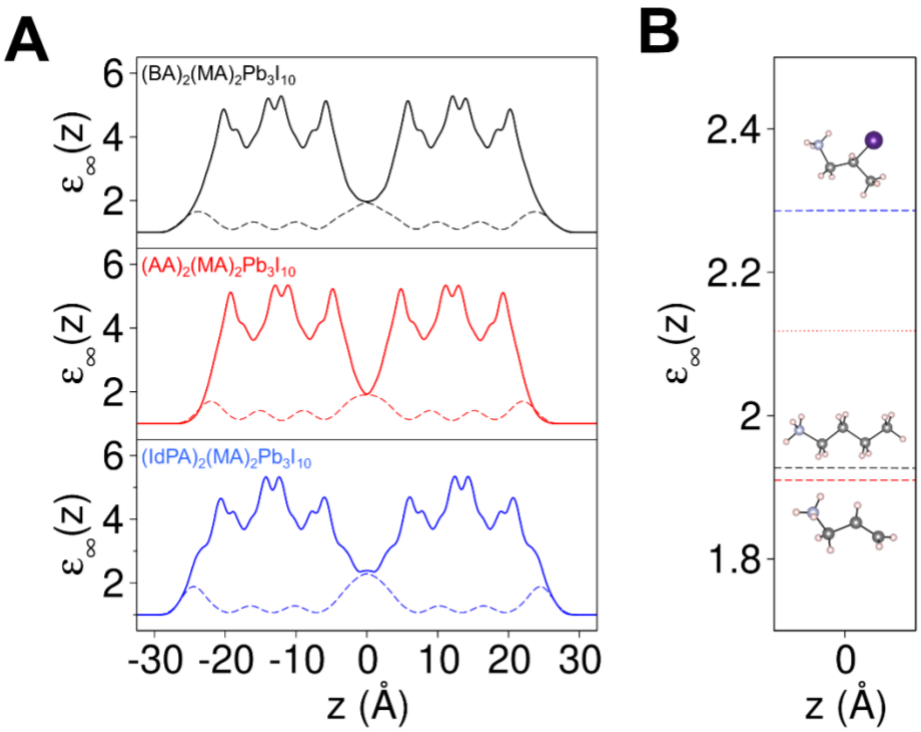

Figure 9. A) Computed high-frequency dielectric constant profile along the stacking axis for $(BA)_2(MA)_2Pb_3I_{10}$ (black solid line), $(AA)_2(MA)_2Pb_3I_{10}$ (red solid line) and $(IdPA)_2(MA)_2Pb_3I_{10}$ (blue solid line). For each compound, the contribution of the organic cations alone is given in black, red and blue dashed lines, respectively. (**B**) Zoom-in on the organic cations AA, IdPA and BA contribution. The red dotted line marks the contribution from a AA cation with a the unsaturated bond oriented perpendicular to the stacking axis which enhances the dielectric response (See **Figure S16**).

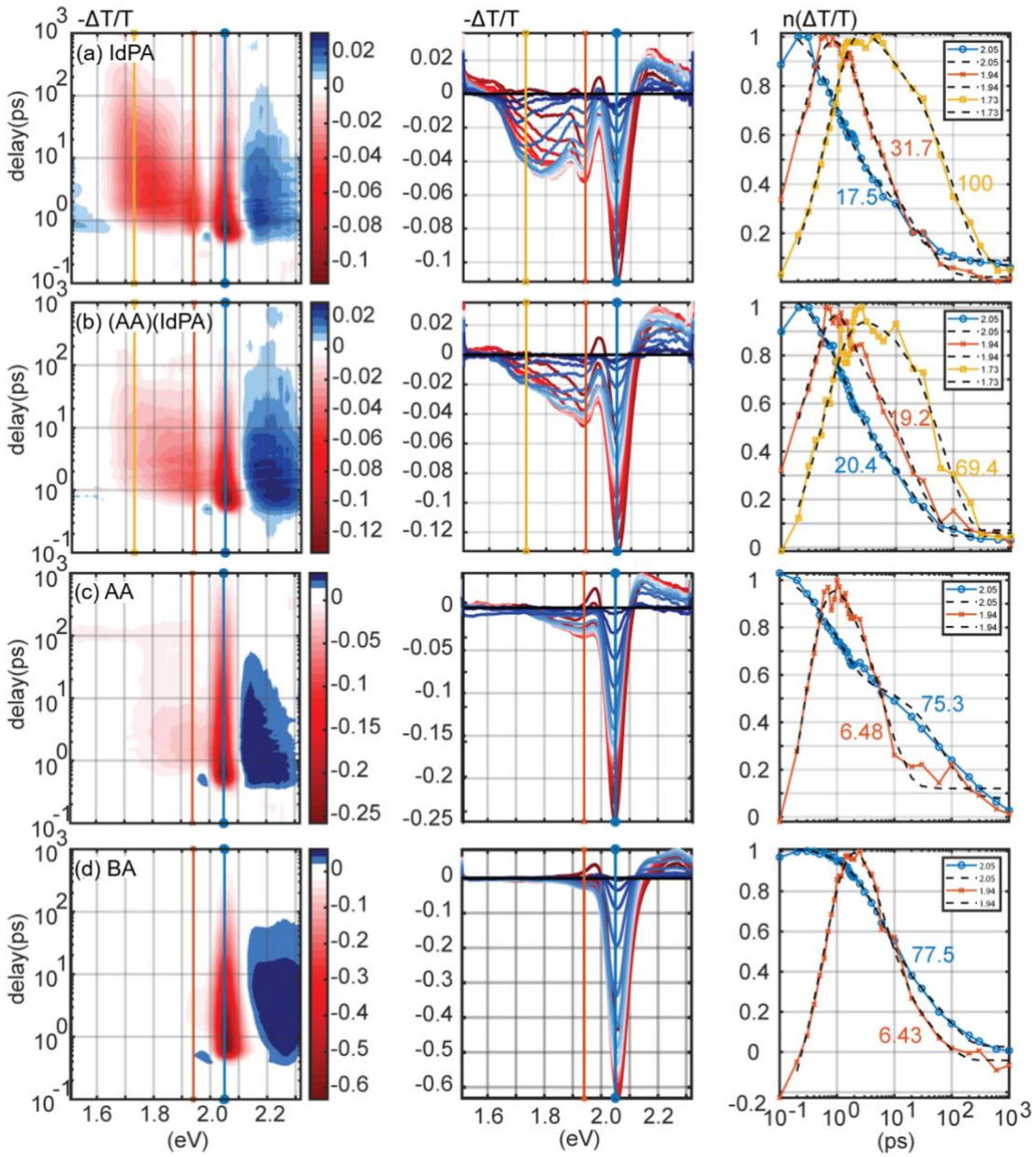

Figure 10. Excited state dynamics of the n=3 allylamine 2D perovskite series with varying IdPA concentration. (Left) Transient absorption surface of IdPA, (AA)(IdPA), AA and BA n=3 crystals. Different levels of signal intensity are plotted as a function of probing energy (x-axis) and delay time after excitation at 2.41 eV (y-axis). Red represents the negative bleaching signal and blue represents the positive absorption signal. (Middle) Transient absorption spectra at different time delays from 0 (red) to 1 ns (blue). (Right) Normalized TA signal intensity at representative energy (each probing energy is marked using a colored line in the left and middle column with the corresponding color). The longest decay lifetimes in picosecond (assigned to be the carrier recombination lifetimes) were extracted using multi-exponential fits and marked near the cuts.

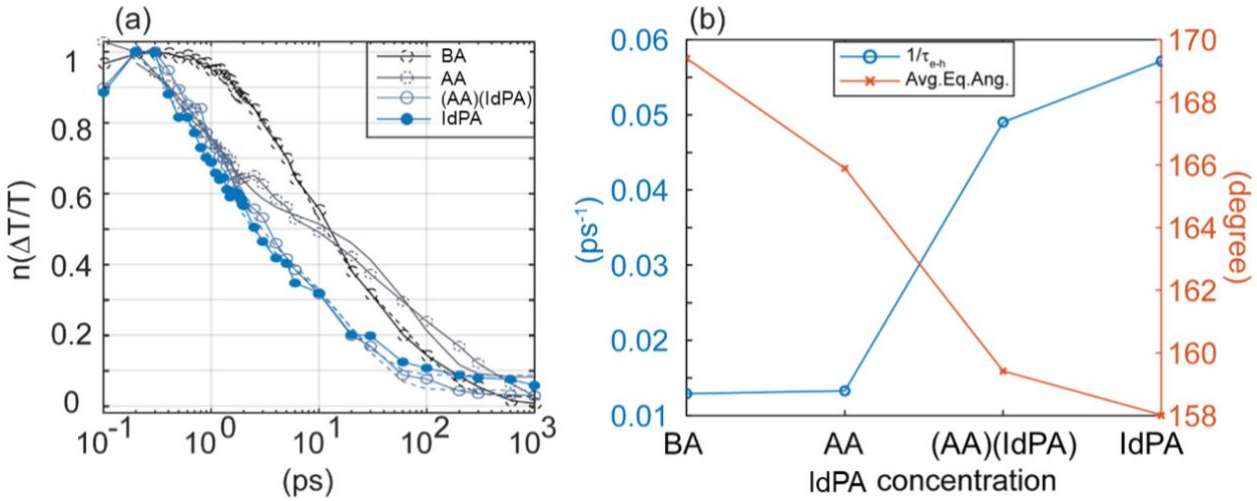

Figure 11. (**A**) The normalized TA signal intensity extracted at the bandgaps showing the recombination dynamics at the bandgaps of crystals containing different cations. (**B**) The correlation between the lattice distortion and recombination lifetimes. The left axis shows the speed of the recombination and the right axis shows the average equatorial Pb-I-Pb bond angle solved by x-ray crystallography indicating the level of distortion inside the inorganic structures. A clear negative correlation can be observed between the level of distortion and the speed of recombination, suggesting the direct effect of lattice distortion on excited-state dynamics.

TOC

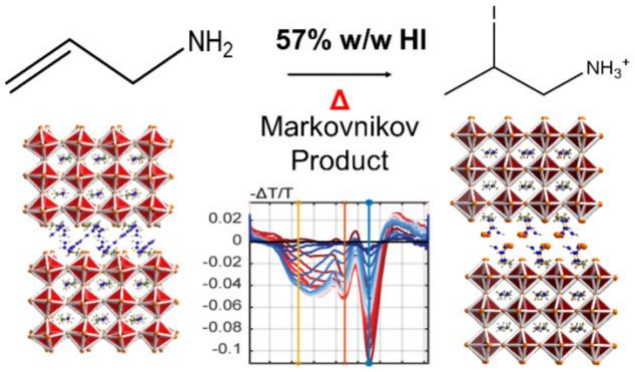
NH2
57% w/w HI
Δ
Markovnikov
Product
I
NH3+
-ΔT/T
0.02
0
-0.02
-0.04
-0.06
-0.08
-0.1